We are IntechOpen, the world's leading publisher of Open Access books Built by scientists, for scientists

6,900
Open access books available

185,000
International authors and editors

200M
Downloads

154
Countries delivered to

Our authors are among the

TOP 1%
most cited scientists

12.2%
Contributors from top 500 universities

BOOK CITATION INDEX
CLARIVATE ANALYTICS
INDEXED

WEB OF SCIENCE™

Selection of our books indexed in the Book Citation Index
in Web of Science™ Core Collection (BKCI)

Interested in publishing with us?
Contact book.department@intechopen.com

Synthesis and Characterization of CMK Porous Carbons Modified with Metals Applied to Hydrogen Uptake and Storage

Marcos B. Gómez Costa, Juliana M. Juárez and
Oscar A. Anunziata

Additional information is available at the end of the chapter

Abstract

In this chapter, we have shown that hopeful hydrogen storage material can be obtained by ordered mesoporous carbons (carbons mesostructured from Korea, CMK-1 and CMK-3) and modified with metal/cations species. The pristine CMK-1 and CMK-3 were synthesized by replication using MCM-48 and SBA-15 as hard templates and sucrose as a carbon source. Incorporation of metal species was carried out by wetness impregnation. The mesoporous materials modified were characterized by X-ray diffraction (XRD), X-ray photoelectron spectra (XPS), RAMAN, transmission electron microscopy (TEM), and adsorption/desorption N_2 isotherms. Carbon modified with metal/cations shows a better capacity for hydrogen uptake than that of the mesoporous carbons. The evolution of high-pressure hydrogen adsorption measured at 77 K shows that composites can significantly enhance hydrogen adsorption capacity and hydrogen storage performance of carbon materials, proving to be prospective candidates for application in hydrogen storage. The improved activity and the larger performance of composite materials are attributed to improved dispersion of uniform metal/cations nanoparticles as well as to efficient use of the support, which may originate a high-surface area and pore volume, allowing a large dispersion of clusters.

Keywords: mesoporous materials, nanocomposites, modified CMK, characterization, hydrogen storage

1. Introduction

Hydrogen is considered as a clean energy carrier and an alternative fuel source for many applications. Some keys to use hydrogen, as a fuel, are its safe storage, low cost, lightweight, and it reversibility, with a simple adsorption-desorption kinetics.

The great challenge posed by the use of hydrogen as an energy source today is primarily focused on the need for safe and stable storage. Its capacity as an energy carrier is demonstrated by its increased energy per mass, cleanliness and ease of production from renewable sources, as opposed to fossil fuels [1]. Thus, a viable solution for both storage and transport problems is required, since alternatives such as hydrogen liquefaction or compression present difficulties due to its low storage density and the high costs involved [1].

Many activated and templated carbons with high-surface area exhibit potential for storing molecular hydrogen [1–4]. Their small weight, low cost, and wealth of natural precursors make nanostructured carbons with high-surface area likely candidates for physisorption. The literature reports that activated carbons show relatively high hydrogen storage capacity at 77 K [2, 3]; however, pore size distribution is in most cases wide, and more than 50% of the total porous volume is given by macropores, whose contribution to hydrogen uptake is more limited.

Carbons mesostructured from Korea (CMK) comprise one such family of ordered mesoporous carbons (OMC) [5]. Produced inside the channels of mesostructured silicates or aluminosilicates, CMK have specific surface areas from 1000 to 2000 m^2/g and pore volumes from 0.5 to over 1 ml/g. These materials are promising for hydrogen storage applications. The template method was used to obtain the carbons, involving first introduction of the appropriate carbon precursors into the ordered template pores and then carbonization and removal of the template. Such carbon materials are characterized by large surface areas and high pore volumes, which make effective H_2 physisorption feasible.

However, a common limitation is found in weak van der Waals interaction between molecular hydrogen and host material. Hence, to enhance hydrogen binding, low amounts of transition metals or cations are added, improving hydrogen sorption [6–9].

Thus, CMK-1 and CMK-3 were chosen as ideal support material for hydrogen storage due to their large surface area, high chemical stability, uniform pore diameter, accessible porosity, and three-dimensional conducting network [10,11].

The scattering of metal particles throughout the porosity of active carbons greatly enhances their storage abilities. Numerous studies devoted to this feature have given ample evidence of hydrogen spillover. H_2 dissociation is supposedly triggered by the catalyst, with atomic hydrogen diffusing deeper into the microporous network and even in between graphitic layers [12].

Nanometric clusters of Pt, Zn, Ni, V, and TiO_2 dispersed in CMK-1 or CMK-3 framework have been reported as promising hydrogen storage nanomaterials. The adsorption in these materials was fully reversible and higher than that in carbon hosts [12,13].

Nanocluster activity improved hydrogen adsorption molecules, producing substantial changes in hydrogen sorption properties.

2. Material and methods

2.1. Templates preparation: MCM-48 and SBA-15

The mesoporous material MCM-48 was prepared as the template for the CMK-1. The meso-porous silicate was synthesized by hydrolysis of tetraethylorthosilicate (TEOS, 98%, Sigma–Aldrich) at room temperature, in an aqueous solution, using cetyltrimethylammonium bromide (CTAB, Sigma–Aldrich) as a surfactant. The procedure designed is described as follows: Sodium hydroxide (NaOH, Sigma–Aldrich) and CTAB were dissolved in deionized water, and then tetraethyl orthosilicate (TEOS) was added. The molar composition of the gel was 1 M TEOS: 0.48 M NaOH: 0.48 M CTAB: 55 M H_2O. After stirring for about 1 h, the solution was transferred into a Teflon bottle and there it was heated up to a temperature of 373 K. After 72 h, the mixture was kept at RT and a solution of HCl was used to turn the pH to 7. Afterwards, the solution was kept at 373 K for 72 h. In order to wash and dry the product, the solution was filtered [14]. The template was extracted by thermal treatment performed up to 373 K, using N_2 (20 mL/min) and afterwards a calcination at 723 K was implemented, raising the tempera-ture 3 K/min [15].

Ordered mesoporous silica SBA-15 was prepared using the triblock copolymer, poly(ethylene glycol)-block-poly(propylene glycol)-block-poly (ethylene glycol), ($EO_{20}PO_{70}EO_{20}$, P123-Sigma–Aldrich), as surfactant, and tetraethyl orthosilicate (TEOS, Sigma–Aldrich, reagent grade 98%) as the source of silica. The technique planned was: A solution was prepared with P123 (20 g) in 400 ml of HCl 1 M at 323 K. Then, TEOS (40 g) was drop under stirring during 24 h at the same temperature. The subsequent white combination was moved to a propylene flask and matured by 72 h at 373 K. The material was filtered out and then washed with deionized water until pH ~ 6. Its molar composition was 1 Si:0.018 $EO_{20}PO_{70}EO_{20}$:2.08 HCl:112 H_2O. The template was removed by immersing the material in ethanol reflux for 6 h and then calcining it at 823 K in air for 6 h. The product was finally filtered, washed, and dried in air at 363 K [16].

2.2. Synthesis of the replicas CMK-1 and CMK-3

Mesoporous carbons CMK-1 and CMK-3 were prepared via a two step impregnation of the mesopores of MCM-48 and SBA-15 with a solution of sucrose using an incipient wetness method. Briefly, 1.0 g of the as-prepared silica material MCM-48 for CMK-1 and SBA-15 for CMK-3 was soaked with 1.1 g of sucrose and 0.14 g of H_2SO_4 in 5.0 g of deionized water solution. The mixture was then dried at 373 K for 6 h and then at 433 K for 6 h. The silica sample, which now contained partially polymerized and carbonized sucrose, had 0.65 g of sucrose, 90 mg of H_2SO_4, and 5.0 g of deionized water added to it, and was treated again at 373 K and 433 K. To complete the carbonization, the sucrose-silica composite was heated at 1173 K for 4 h under nitrogen flow (20 mL/min).

The silica template was dissolved with 5 wt% hydrofluoric acid at room temperature. This step was done two times in order to dissolve entirely the template. The template-free carbon product thus obtained was filtered, washed with deionized water and ethanol, and dried [12, 13].

2.3. Synthesis of Zn-CMK-1

Zn-CMK-1 was prepared using as a source of zinc Zn nitrate (Sigma–Aldrich 98%, hexahydrate), dissolved in ethanol, and then mixed with a portion of CMK-1 at room temperature. The suspension was left static for 24 h, before being dried at 373 K for a period of 18 h, and subsequently desorbed from 298 K to 473 K in an inert atmosphere (N_2), at a rate of 10 K/min. It was held at this latter temperature for 5 h. During the whole process, the nitrogen flow was 20 ml/min. To obtain the reduced sample of Zn-CMK-1, it was placed under H_2 flow at 773 K for more than 6 h with a ramp rate 10 K/min. The sample was denoted as Zn-CMK-1. ICP analysis showed that the pristine sample of Zn-CMK-1 contained 5.5 wt% of Zn before reduction and 5 wt% afterwards [13].

2.4. Synthesis of Ni-CMK-1

Ni-CMK-1 was obtained by impregnating CMK-1 using $NiCl_2.6H_2O$ (Sigma–Aldrich 98%) dissolved in ethanol, which was stirred vigorously for 20 min. Then, the sample was dried under vacuum at 308 K, to achieve complete dryness by evaporation of the solvent. The powder obtained was heated to 353 K to dry and then placed in a tubular furnace at 773 K under controlled flow of H_2 for reduction during 6 h. It was determined by ICP that the reduced sample contained 5.5 wt% Ni [13].

2.5. Synthesis of Pt-CMK-3

The sample was prepared by wetness impregnation using chloroplatinic acid ($H_2PtCl_6 \cdot H_2O$-Sigma–Aldrich) as Pt source. Chloroplatinic acid in ethanol was added to the carbon solution at room temperature. Excess of ethanol was removed by placing the solution in a rotary evaporator at around 333 K and 60 revolutions per minute. The sample was then dehydrated at 373 K during 18 h. The resultant solid was heated under nitrogen flow from 298 K to 473 K (ramp 10 K/min) and maintained at 473 K for 5 h. Afterwards, it was heated up to 743 K (slope 10 K/min), where it was kept for another 5 h. The nitrogen flow was kept constant at 20 ml/min. The sample was also subjected to H_2 flow at 773 K for 6 h with a ramp rate of 10 K/min. The sample was denoted as Pt-CMK-3. 1% wt of Pt in the final Pt-CMK-3 material was obtained [12].

2.6. Synthesis of TiO2-CMK-3

TiO_2 nanoparticles were incorporated into ordered mesoporous carbon CMK-3 using wetness impregnation and tetrabutyl orthotitanate (TBOT) as a titanium source. The metal precursor

(TBOT) was dissolved in 10 mL of ethanol with vigorous stirring, to reach a nominal content of 5 wt% of Ti in the final solid. CMK-3 was incorporated in the solution, and both were placed in a rotary evaporator to remove excess of ethanol at about 313 K and 60 rpm. The powder was then dried at 373 K overnight. Finally, the resulting material was heated in a dynamic inert atmosphere (nitrogen flow of 20 mL/min) from 298 to 473 K with a slope of 4 K/min; temperature was then increased to 743 K with a slope of 10 K/min and kept at this temperature during 5 h.

2.7. Synthesis of V-CMK-3

Vanadium nanoparticles were incorporated into ordered mesoporous carbon CMK-3 using wetness impregnation and VCl_3 as source of Vanadium. The metal precursor (VCl_3) was dissolved in 20 mL of ethanol with vigorous stirring, to have a nominal content of 1 wt% of V in the final solid. The solution was placed in a rotary evaporator to remove excess of ethanol at about 323 K and 50 rpm. The obtained powder was then dried at 373 K overnight. The resulting material was heated in a dynamic inert atmosphere (nitrogen flow of 20 mL/min) from 298 to 473 K with a slope of 4 K/min, and then, the temperature was increased to 743 K with a slope of 10 K/min and kept at this temperature during 5 h. A reduction procedure in H_2 flow (20 mL/min) was performed to the sample at 1023 K using the same procedure described earlier.

2.8. Characterization of the samples

ICP (ICP-AES; VISTA-MPX) was used to determine the elemental composition, working at a frequency of 1.5 kW under airflow 12 L/min. In order to determine textural properties, such as surface area and pore volume, N_2 adsorption/desorption isotherms at 77 K were measured on ASAP 2020. To realize studies of the adsorption isotherms, the samples were purged at 673 K, and size pore distribution assessed by means of Barrett, Joyner, and Halenda (BJH) algorithm. The hydrogen chemisorption characterization was realized in the Micromeritics Chemisorb 2720 apparatus, equipped with a detector TCD, at RT. The cleaned samples were titrated with H_2 pulses at 295 K under flow of N_2 up to a persistent output signal of TCD, which indicates saturation.

X-ray diffraction profiles of samples were recorded with a X'PertPro PANalytical diffractometer equipped with a Cu Kα radiation (λ = 0.154 nm, X-ray generator current and voltage set at 40 mA and 45 kV). The samples were crushed previously and placed on an aluminum sample holder. The diffraction patterns were recorded in steps over a range of Bragg angles (2θ) between 0.5° and 5° (and for wide angle between 20 and 70°), at a scanning rate of 0.02 per step and an accumulation time of 20 s. Diffractograms were analyzed with the X'Pert High Score Plus software. X-ray photoelectron spectra (XPS) were obtained on a Microtech Multilb 3000 spectrometer, furnished with a hemispherical electron analyzer and MgKα (hν = 1253.6 eV) photon source. An estimated error of ±0.1 eV can be obtained for all ranges. Peak intensity was determined from each peak areas after background removal and spectrum suitable by a combination of Gaussian/Lorentzian functions. Surface relation ratios (50–100 A of Deep) were

extracted as a function of the intensities of the signals corrected by the sensitivity factors with an estimated precision of ±7%.

Raman spectrum was acquired from an InVia Reflex Raman microscope and spectrometer using a 532 nm diode laser excitation. The transmission electron microscopy (TEM) micrographs were recorded in a Philips EM 301, with accelerating voltage of 200 kV (point resolution of 0.17 nm).

To determine hydrogen storage isotherms, we employed an ASAP 2050 apparatus properly calibrated, at 77 K and at low and high pressures (up to 10 bar). Previous to all the adsorption experiments, the samples were degassed at 523 K during 8 h under vacuum conditions, to prevent the probable decomposition of the metal nanoparticles at higher temperature. Afterwards, the samples were cooled at RT. The adsorption experiments were carried out with high-purity hydrogen gas (99.9999%), and in a pressure range from 0 to 10 bar.

3. X-ray diffraction studies

Figure 1 shows typical XRD patterns for the MCM-48 silica template and the carbon CMK-1 produced with the aforementioned procedures. The low-angle XRD pattern of MCM-48 points to a high degree of structural order for the cubic crystallographic space group Ia3d (**Table 1**). However, a different pattern relative to MCM-48 can be observed for the carbon CMK-1, obtained by removing the silica wall after carbonization. As opposed to CMK-2, 3, and 4, the structure of the CMK-1 obtained through the use of silicate MCM-48 templates was not found to be an exact negative replica of the template. This was due to a transformation of the mesostructure after the template wall had dissolved. This structural transformation was mainly evidenced by the appearance of a strong low-angle diffraction peak (h k l [1 1 0] at 2θ = 1.67°) on the X-ray diffraction (XRD) patterns of CMK-1 (see **Figure 1**), which was not reliable with the symmetry of MCM-48 [12,17].
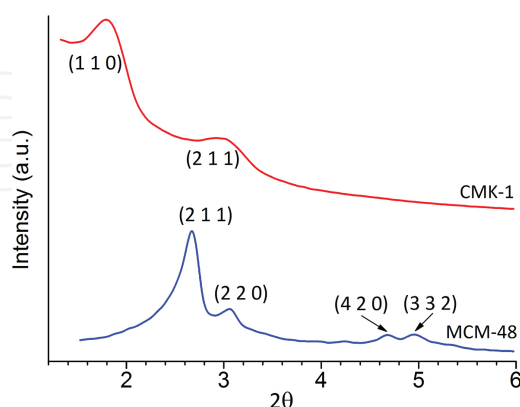

Figure 1. Small-angle XRD patterns of MCM-48 and CMK-1.

As shown by the low-angle powder XRD pattern, a structural transformation of the interlaced carbon framework occurs after the silica wall has dissolved. A displacement of the

sub-frameworks with respect to each other may lead to the formation of contacts. A distortion of the frameworks may also take place as a consequence of further transformations. The principal indicator of structural transformation of the material is the strong low-angle diffraction peak appearing in the XRD powder pattern, which is inconsistent with the space group Ia3d of the MCM-48 template. This reflection is indexed as [1 1 0], and the explanation of its emergence may lie in a decrease in the material symmetry. The complexity of the framework structure of CMK-1 is such that it fails to be described by simple terms such as "pore," "wall," or "diameter," which are commonly used in descriptions of the texture of mesoporous materials and molecular sieves. However, an estimation of its geometric characteristics might be in place. It is possible to determine the diameter of the roughly cylindrical framework segments, which coincide with the Wyckoff symmetry positions 12c and 12d of the I_41_{32} space group [18].

Sample	MCM-48 (h k l)			CMK-1 (h k l)			a_0 (nm)
	2 1 1	2 2 0	4 2 0	3 3 2	1 0	2 1 1	
	d (nm)			d (nm)			
Si-MCM-48	3.71	3.21	2.02	1.93	–	–	9.1
CMK-1	–	–	–	–	5.85	3.35	8.2
Zn-CMK-1	–	–	–	–	5.59	–	7.9
Ni-CMK-1	–	–	–	–	5.78	3.32	8.2

Table 1. XRD parameters of samples.

Figure 2 shows the low-angle X-ray diffraction patterns of CMK-1, Ni-CMK-1, and Zn-CMK-1 samples. Retention of the overall pore structure after the addition of the different metals is indicated by the low-angle diffraction peaks (Table 1). However, the peak intensity of the samples is noticeably lower than that of the parent CMK-1. This intensity loss may be due to the introduction of scattering material into the pores, leading to an increased phase cancellation
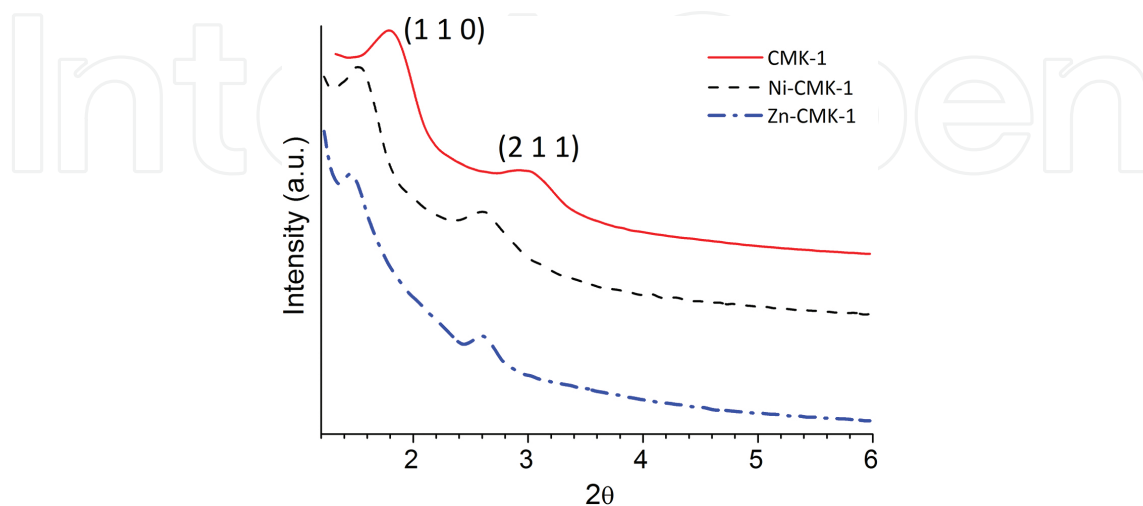

Figure 2. Small-angle XRD patterns of CMK-1, Ni-CMK-1, and Zn-CMK-1.

between scattering from the walls and the pore regions [19]. In the case of the Zn-CMK-1 sample, the absence of XRD reflections can be ascribed to a very high degree of pore filling.

Figure 3 shows a typical XRD pattern for the silica template SBA-15 and the carbon CMK-3 yielded by the procedures described. The low-angle XRD pattern of SBA-15 points to a high degree of structural order for the hexagonal P_6mm crystallographic space group (**Table 2**). A similar pattern relative to SBA-15 can be observed for the carbon CMK-3 obtained by removing the silica wall after carbonization. The structure of the CMK-3 obtained by the use of a silicate SBA-15 template was found to be an exact negative replica of the template. The structural transformation was mainly evidenced by the appearance of CMK-3 on the X-ray diffraction (XRD) patterns, which was consistent with the symmetry of SBA-15 [19].
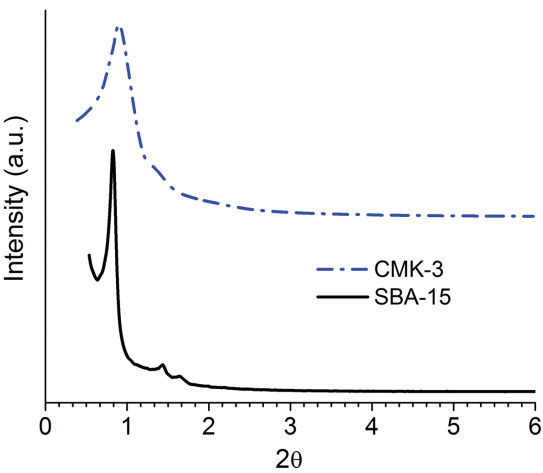

Figure 3. Small-angle XRD patterns of SBA-15 and CMK-3.

Sample	SBA-15 [h k l]			CMK-3 [h k l]			a_0 (nm)
	[1 0 0]	[1 1 0]	[2 0 0]	[1 0 0]	[1 1 0]	[2 0 0]	
	d (nm)			d (nm)			
SBA-15	8.6	5.0	4.3	–	–	–	10.0
CMK-3	–	–	–	10.5	6.1	5.2	12.1
Pt-CMK-3	–	–	–	8.4	4.9	4.2	9.70
TiO$_2$–CMK-3	–	–	–	7.1	4.4	3.8	8.60
V-CMK-3	–	–	–	7.2	4.2	3.9	8.50

Table 2. XRD parameters of samples.

Figure 4 shows the low-angle X-ray diffraction patterns of CMK-3 and of the modified samples. The overall pore structure is retained after the addition of Pt, TiO$_2$, and V, which is indicated by the low-angle diffraction peaks (**Table 2**). However, the signal intensity corresponding to the [1 1 0] diffraction plane of the samples shows a slow decrease in relation to the parent

CMK-3. The introduction of scattering material into the pores generally leads to an increased phase cancellation between scattering from the wall and the pore regions. The intensity loss of CMK-3 typical Bragg reflections is caused by the introduction of scattering material (Pt, TiO_2, and V) into the pores [19].
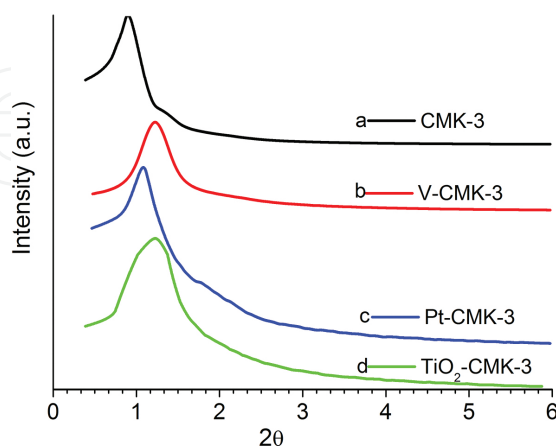

Figure 4. Small-angle XRD patterns of CMK-3 (a), V-CMK-3 (b), Pt-CMK-3 (c), and TiO_2–CMK-3 (d).

Figure 5 shows the wide-angle diffraction region of the Zn-modified sample (Zn-CMK-1). XRD pattern at the wide-angle range (10–60°) of the CMK-1 host (see the inset of **Figure 5**) exhibits two broad diffraction peaks which can be indexed as [0 0 2] and [1 0 0] diffraction for typical graphite carbons [20].

The pattern of Zn-CMK-1 shows ZnO and metallic Zn signals [21,22], probably due to the reduction process not being complete. The fact that this pattern exhibits no prominent reflections is an indicator that no crystalline bulk material was formed outside the pore system. The Zn/ZnO clusters are confined for the most part in the nanostructured carbon [23], showing nanometric size and high dispersion which can be seen in **Table 1** and TEM studies.
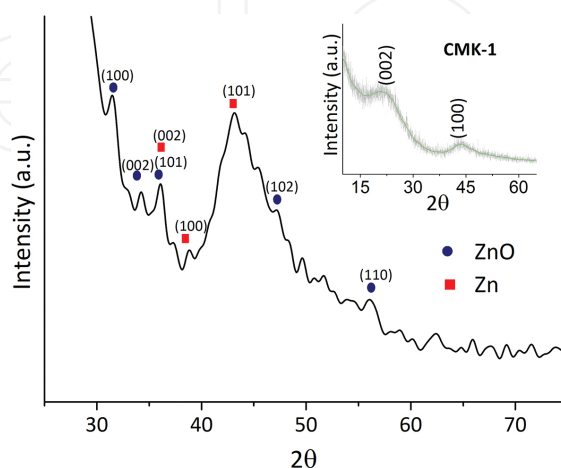

Figure 5. Wide-angle XRD patterns of Zn-CMK-1 and CMK-1 (inset).

The XRD pattern of Ni-CMK-1 (**Figure 5**) shows intensive peaks at 2θ = 44.5, 51.8, and 76.3°, corresponding to metallic Ni diffraction planes [1 1 1], [2 0 0], and [2 2 0], [45]. These are characteristic patterns of an fcc lattice consisting of nickel nanoparticles. NiO species may be present, since the NiO signals were very close to metallic Ni signals and would overlap [24] in the pattern, as TEM-EDS and XPS studies will show later. In agreement with XRD studies, the characteristic structure of CMK-1 is maintained after the metal is within the host, whereas the nanomaterial area becomes significantly smaller (**Table 1**).

Figure 6 displays the diffraction region of 20–70° 2Θ of samples. Typical XRD pattern of mesoporous materials was exhibited by SBA-15 sample. Two broad diffraction peaks were found in CMK-3 pattern which can be ascribed to [0 0 2] and [1 0 0] diffraction indexes for a characteristic graphite carbons [20].

The final sample of Pt-CMK-3 pattern displays metallic platinum peaks [25], pointing to a well-developed reduction process. In the case of Pt clusters, the absence of prominent reflections indicates that no crystalline bulk material formation had occurred outside the pore system [23], with nanometric size and high dispersion (very broad XRD signal of Pt, **Figure 6**) as shown in **Table 2**. The reason for this may be found in a relatively low scattering contrast between the pores and the walls of the mesoporous materials caused by the formation of reduced platinum which indicates fine dispersion on CMK-3 with a narrow size distribution [24].
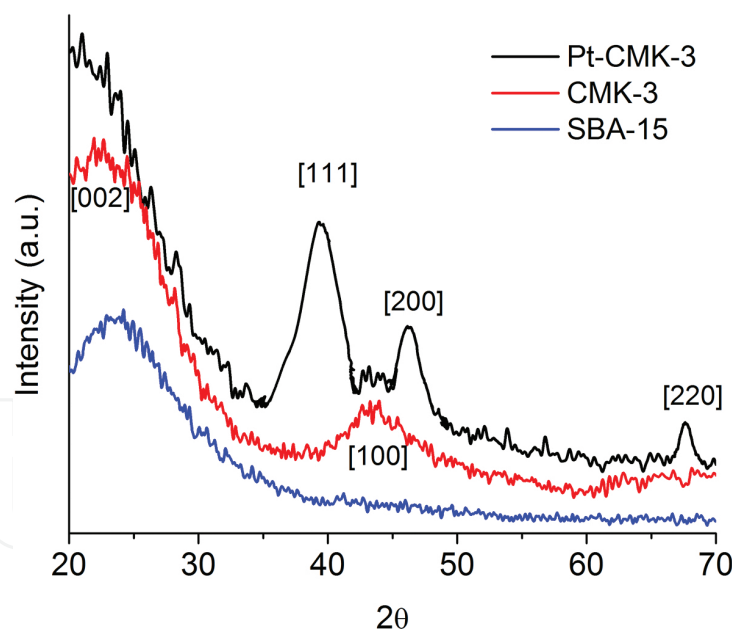

Figure 6. Wide-angle XRD patterns of SBA-15, CMK-3, and Pt-CMK-3.

Figure 7 shows the wide-angle X-ray diffraction patterns for CMK-3 and TiO_2-CMK-3. In both cases, two broad diffraction peaks are distinguished, which can be indexed as [0 0 2] and [1 0 0] diffraction for typical graphite carbons [20].

The pattern of TiO_2-CMK-3 shows characteristic signals of TiO_2 in anatase phase [26], indicating a particularly good synthesis process. The absence of prominent reflections in TiO_2 clusters

indicates that no crystalline bulk material has been formed [23], with nanometric size and high dispersion (very broad XRD TiO$_2$ signals, **Figure 7**). This can be ascribed to a relatively low scattering contrast between the pores and walls of mesoporous materials, due to the formation of anatase nanoclusters that depict fine dispersion on CMK-3 with a narrow size distribution [24].
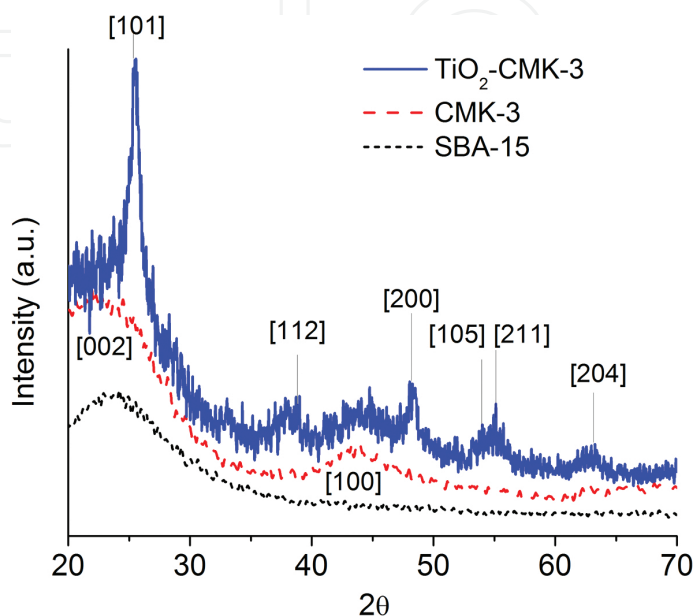

Figure 7. Wide-angle XRD patterns of SBA-15, CMK-3, and TiO$_2$–CMK-3.

Figure 8 shows the wide-angle X-ray diffraction patterns for CMK-3 and V-CMK-3. In both cases, two broad diffraction peaks are distinguished which can be indexed as [0 0 2] and [1 0 0] diffraction for typical graphite carbons [20].
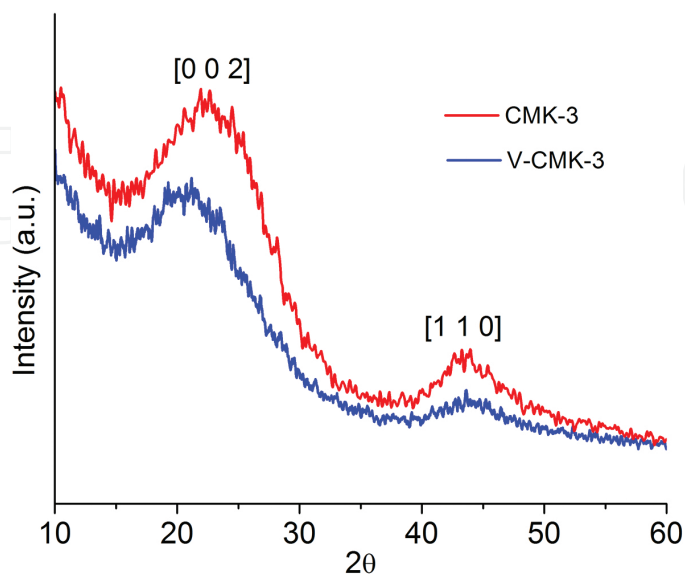

Figure 8. Wide-angle XRD patterns of CMK-3 and V-CMK-3.

In the wide-angle region, practically no reflections typical of vanadium have been found. The absence of these prominent reflections indicates that no crystalline bulk materials have been formed outside the pore system and it is an evidence that the clusters have nanometric size and high dispersion [23].

3.1. Cluster size estimation using Scherrer's formula

Analysis of the XRD patterns makes it possible to determine the size of crystals of metallic particles in the samples and to evaluate the effect on metal dispersion. The average cluster size was thus estimated based on the width of the diffraction peaks corresponding to different [h k l] Miller indices using Scherrer's formula (Eq. (1)) [27].

$$d = \frac{K\lambda}{\beta \cos\theta} \tag{1}$$

where d is the average size of the crystals or domains (the crystal mean size defined as the cube root of the material volume). K is a shape factor of the nanocluster, dimensionless, generally has a typical value of 0.89 or 0.83 (if the particles are approximately spherical or not), λ is the wavelength of the X-rays (1.54 Å) used for performing the analysis, β is the full width at half-maximum (FWHM, in radians) of the XRD signal, and θ is the Bragg angle (in radians) [28].

In order to apply Scherrer's formula, [1 1 1], [2 0 0], and [2 2 0] refractions plains for Pt-CMK-3 were employed. The average diameter of the metal particles, as obtained by Scherrer's formula, was ~1.76 nm. In the case of TiO_2-CMK-3, the average diameters of anatase particles obtained by Scherrer's formula were ~5 nm, employing [1 0 1], [1 1 2], and [2 0 0] refractions plains.

In the case of the sample CMK-1 modified with Ni, the planes [101], [200], and [220] were used. For the Zn-CMK-1, [100] and [101] refraction planes for Zn^0 and for ZnO the planes [002] and [110] were used. Using Scherrer's formula, the average size of metal nanoclusters for the sample modified with Ni were 13 nm, and 2.3 nm and 2.6 nm for the Zn^0 and the ZnO particles.

4. Nitrogen adsorption/desorption isotherm analysis

Figure 9 shows the N_2 adsorption/desorption isotherms for MCM-48, CMK-1, Zn-CMK-1, and Ni-CMK-1 samples, while **Table 3** shows the textural properties obtained from nitrogen physisorption analysis. The nitrogen adsorption–desorption is other for MCM-48 has a typical type IV curve (according to the IUPAC classification), which is a sure indicator of the meso-porous nature of the material. The isotherm for CMK-1 and Zn-CMK-1 and Ni-CMK-1 shows hysteresis loops at a relative pressure range of 0.4–0.6, which can be caused by capillary condensation-evaporation from the mesopores. Zn-CMK-1and Ni-CMK-1 clearly reveal a reduced specific surface area (as well as a narrowed pore size), as opposed to those of pure MCM-48 and CMK-1 (**Table 2**), with the corresponding incorporated metallic species.
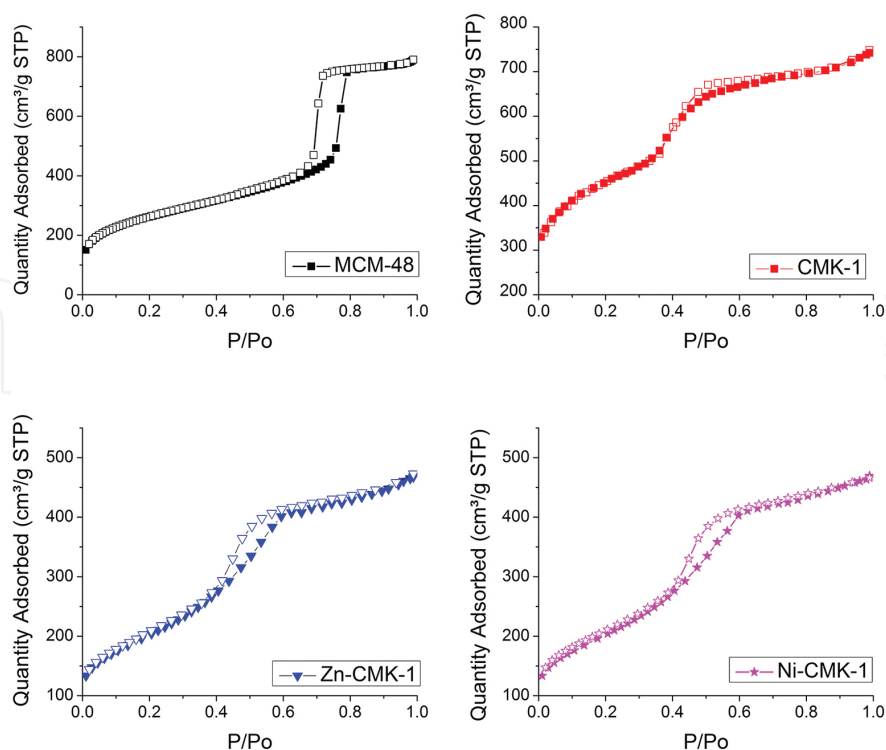
Figure 9. N_2 adsorption–desorption isotherms of MCM-48, mesoporous carbon CMK-1, Zn-CMK-1, and Ni-CMK-1.

Sample	Area (m²/g)	VP (cm³ g⁻¹) mesoporous volume	BJH pore diameter (nm)	Metal cluster average size (nm)*	H₂ sorption (wt%)**
Si-MCM-48	1034	0.96	2.22	–	–
CMK-1	1089	0.69	3.11	–	2.1
Zn-CMK-1	568	0.55	2.65	Zn: 2.3	4.4
				ZnO: 2.6	
Ni-CMK-1	560	0.51	2.50	Ni Ni + NiO: 12	2.4

* Estimated by XRD (Scherrer formula) and TEM.
** H₂ sorption at 10 bar and 77 K.

Table 3. Textural and structural properties of the samples.

The sharp peak at pore size distribution of CMK-1 and Zn- and Ni-containing CMK-1 (**Figure 10**) indicates a fairly regular range of nanopores in carbonaceous materials, in correspondence with TEM observations.

The isotherm for CMK-3 and Pt-CMK-3 samples shows hysteresis loops at a relative pressure range of 0.4–0.8, which may be caused by capillary condensation–evaporation from the mesopores (**Figure 11**). The material appears in the form of fairly uniform carbon rods (see TEM images) with a higher pore volume as a result of the presence of mesopores between

carbon rods. Irregularities (i.e., the presence of a fraction of nonlinear channels) can be attributed to SBA-15 meso-tunnels being incompletely filling with carbon precursor. The pore size distribution of CMK-3 shows a pronounced peak at 4 nm that points to a quite regular array of nanopores.
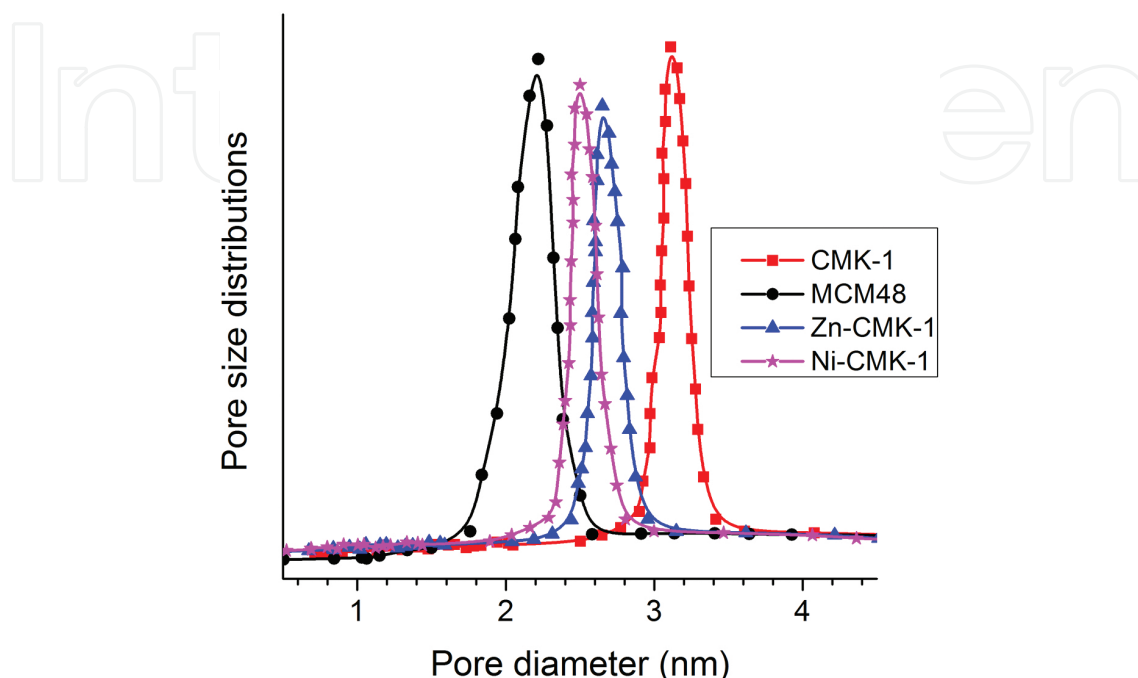

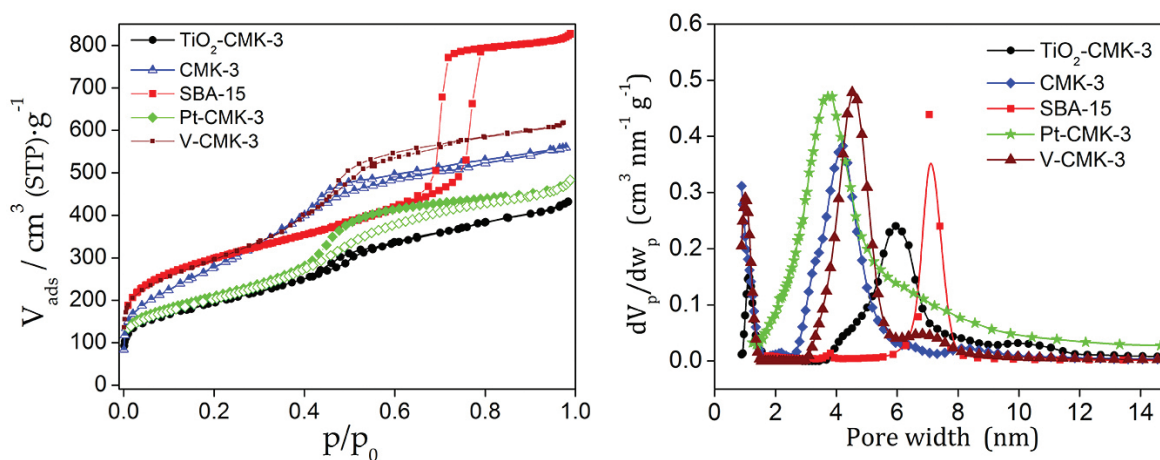**Figure 10.** Pore size distribution of MCM-48, CMK-1, Zn-CMK-1, and Ni-CMK-1.

Figure 11. Nitrogen adsorption (solid symbols)–desorption isotherm (open symbols) at 77 K and pore size distribution of (a): SBA-15, (b) CMK-3, (c) Pt-CMK-3, (d) TiO$_2$-CMK-3, and (e) V-CMK-3.

On the contrary, the Pt-CMK-3 pore size distribution shows a broad peak with a maximum at approx. 3.8 nm, which is consistent with primary mesopores. The appearance of a wide peak can be ascribed to the filling of pores with Pt nanoclusters and the increase in the irregularity

of nanopores. Around 6 nm an overlapping peak appears, corresponding to CMK-3 pores that are not filled with Pt nanoclusters. These analyses of pore size (see **Figure 11**) were consistent with observations from TEM.

Figure 11 also shows, the N_2 adsorption/desorption isotherms for SBA-15, CMK-3 and TiO_2-CMK-3 samples at 77 K; **Table 4** displays the textural properties determined from nitrogen physisorption analysis. The isotherm for SBA-15 is a typical type IV curve with hysteresis loop, according to IUPAC classification, revealing the mesoporous nature of the material.

The nitrogen adsorption/desorption isotherms for CMK-3 and TiO_2-CMK-3 are typical type IV curves exhibiting hysteresis loops type H_2, according to IUPAC classification, typical of mesoporous solids.

The materials obtained exhibit capillary condensation to relative pressures about 0.40 and 0.45, which can be related to the pore blocking effect of influencing pressure where evaporation/desorption pore occurs. The increase in adsorption at low relative pressures is associated with the presence of micropores or a strong adsorbate-adsorbent interaction.

TiO_2-CMK-3 reveals a reduced specific surface area, in comparison with those of pure SBA-15 and CMK-3, with incorporated anatase nanoparticles.

The CMK-3 pore size distribution shows a sharp peak at 4.2 nm that points to a quite regular array of nanopores. On the other hand, the pore size distribution of TiO_2-CMK-3 exhibits a broad peak with a maximum at approximately 6 nm, which is consistent with primary mesopores.

Material	SBET ($m^2 g^{-1}$)	VµP ($cm^3 g^{-1}$)	VTP ($cm^3 g^{-1}$)	Wp (nm)
Pt-CMK-3	500	0.03	0.98	3.8
V-CMK-3	1054	0.16	0.95	4.5
TiO_2–CMK-3	706	0.11	0.67	6.0
CMK-3	1323	0.23	1.01	4.3
SBA-15	1040	0.57	1.38	7.0

VTP, total pore volume; SBET, BET surface area; VµP, micropore volume; Wp, wide mesopore.

Table 4. Textural properties of the materials and composite.

N_2 adsorption/desorption isotherms and pore size distribution for CMK-3 and V-CMK-3 samples at 77 K shown **Figure 11** and **Table 4**, displays the textural properties determined from nitrogen physisorption analysis. The nitrogen adsorption–desorption isotherms for CMK-3 and V-CMK-3 are typical type IV curves exhibiting hysteresis loops type H_2, according to IUPAC classification, typical of mesoporous solids.

Materials obtained exhibit capillary condensation to relative pressures about 0.40 and 0.45, which can be related to the pore blocking effect of affecting the pressure where evaporation/desorption pore occurs. The increase in adsorption at low relative pressures of the samples

CMK-3 instead V-CMK-3 is associated with the presence of micropores or a strong adsorbate-adsorbent interaction.

V-CMK-3 reveals a reduced specific surface area, in comparison with those of pure CMK-3 (**Table 4**), with the corresponding incorporated metallic species.

5. XPS studies

5.1. Ni-CMK-1, Zn-CMK-1, Pt-CMK-3, and V-CMK-3 XPS characterization

Zn-CMK-1 XPS data exhibited that zinc appears as Zn^0 or Zn^{2+} ions (**Figure 12**), according to the binding energies (BE) of Zn ($2p_{3/2}$) electron at 1022.5 eV. The Zn $2p_{3/2}$ spectrum of Zn oxide, though not presenting multiple splitting or other complex effects, overlaps with Zn^0 species peak BE [29]. According to Woll [30], the Zn $2p_{3/2}$ lines for Zn and ZnO are quoted at 1021.4 eV and 1021.7 eV.
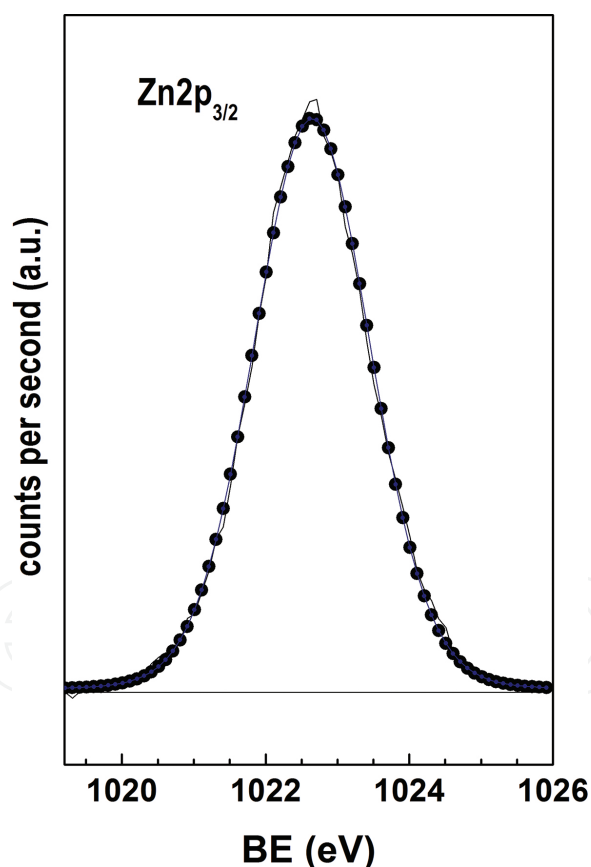

Figure 12. Zn-CMK-1 XPS spectrum.

The split 2p electron energy levels for Ni, Ni ($2p_{1/2}$), and Ni ($2p_{3/2}$) and seemed at 865–885 and 850–865 eV, respectively (**Figure 13**). These bond energies are lower by 1.5–2.0 eV for pure NiO [31]. This abnormality is possibly because the variance in organization of Ni^{2+} in NiO and on

CMK-1. It can confidently be said that Ni^{2+} ions are coordinated in higher symmetry in CMK-1, having a well-ordered crystal structure compared to that of NiO. The satellite band which appears at higher bond energy values also indicates the typical oxide structure.
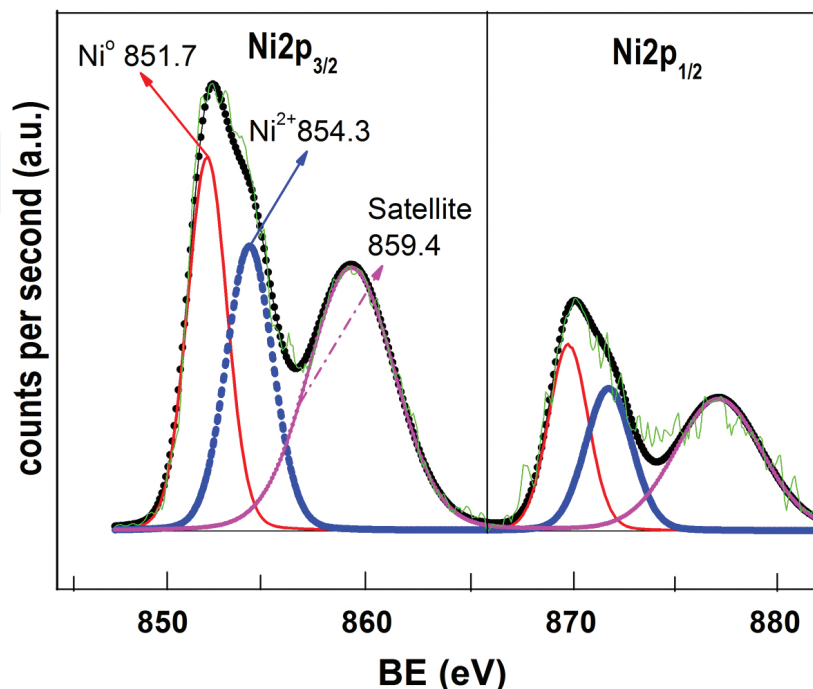

Figure 13. XPS binding energies spectra of the Ni $2p_{3/2}$ and Ni $2p_{1/2}$ peaks region separate by a vertical line. Gaussian component: Ni^0 solid line; NiO dot line and satellite peak of NiO dash dot line.

Activation under H_2 causes a partial reduction of the surface Ni^{2+} species, which yields Ni^0 (reduced catalyst). In addition to Ni^0, the reactive surface contains mixed $Ni^0 + NiO$. The mixed nickel compounds (such as nickel oxides and hydroxides) can appear in relatively large particles, where the NiO compound can be present on the outer surface, and metallic Ni is located in a the sub-surface close to the support, respectively. This distribution can be due to the drastic changes of the deposits' electronic structure that take place as the cluster size increases. Cluster size has a direct impact on the final state in the photoemission process because, once the process is over, the positive charge that remains on the aggregate can be less screened delocalized, compared with an extended metallic system. This entails a shift of the XPS spectrum corresponding to the Coulomb energy of localized charge. The shift proved to be proportional to the reciprocal particle diameter [32]. As a consequence, the binding energies of small metal aggregates should be found at higher values, as was in fact observed in a large number of cases. Elemental XPS analysis (Zn $2p_{3/2}$. O1s and C1s) showed that the chemical composition for Zn, O, and C, 0.2 %, 0.16%, and 99.64% (at.%), respectively, at 50–100 Å of depth for Zn-CMK-1 sample. Nevertheless, EDS study (**Figure 18c** and **d**) showed that the Zn content was 4.85 wt%, which suggests the Zn^0 (74%) lies inside the mesoporous of CMK-1 sample. Furthermore, by XPS, the oxygen concentration was around 80%, giving support to the knowledge that the ZnO lie on the external Zn-CMK-1 surface.

XPS study of Ni-CMK-1 point to a composition for Ni, O, and C as follows: 0.625, 0.375, and 99 (at.%), whereas by EDS analysis (5.3 and 0.6 wt% and for Ni and O, respectively). Therefore, a large amount of NiO is located on the outside of CMK-1 (>40%), consistent to the inferior quantities of Ni^0 create in Ni-CMK-1 mesoporous material. The EDS and XPS studies for Zn and Ni support the difference in cluster size obtained by XRD (Scherrer's formula) and TEM, shown in **Figure 18a** and **b** (2.5 nm and 12 nm, respectively). This is an indicator that the nanostructure of CMK-1 prevents the growth of large crystals in its nanopores, especially during the addition of zinc.

The XPS technique is normally used to determine the nature and oxidation state of Pt species (Pt^0, Pt^{2+}, and Pt^{4+}), and in particular the Pt (4f) peak study is employed (**Figure 14**). Metallic Pt^0 is known to have binding energies of 70.7–70.9 and 74.0–74.1 eV for $4f_{7/2}$ and $4f_{5/2}$ electrons, respectively [33]. In oxidized states, the binding energies exhibited by Pt^{2+} and Pt^{4+} are much higher: 72.8–73.1 eV ($4f_{7/2}$) and 76.3–76.4 eV ($4f_{5/2}$) for Pt^{2+} and 74.6–74.9 eV ($4f_{7/2}$) and 78.1–78.2 eV ($4f_{5/2}$) for Pt^{4+} [34].
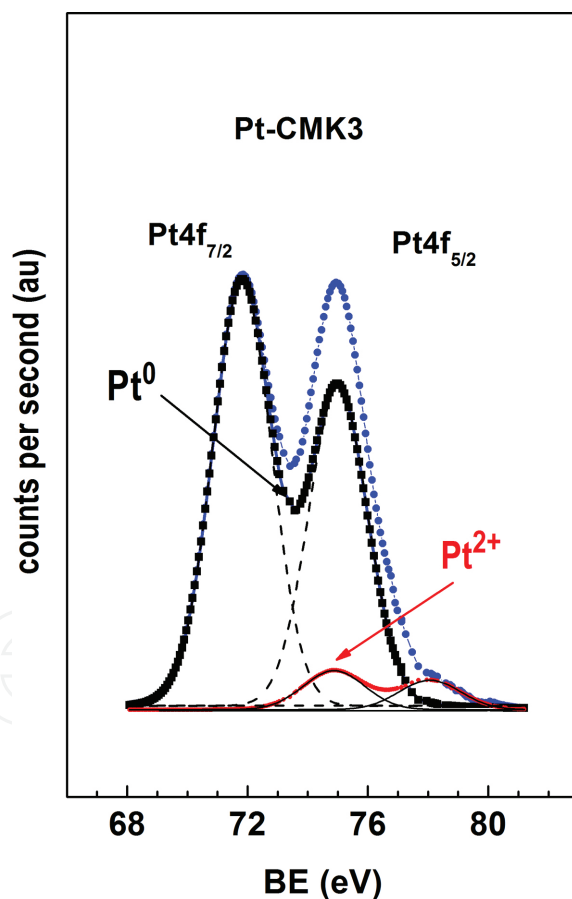

Figure 14. Core level Pt4f XPS spectra of Pt-CMK-3.

The spectra showed two pairs of peaks. As we can see all spectra displays signals at low and high energy (doublets), Pt $4f_{7/2}$: 71.8 eV and $4f_{5/2}$: 75.1 eV, demonstrating that Pt nanoclusters are metallic (**Figure 14**). The Pt^0 peak moves slightly to higher binding energies; this

phenomena is in agreement to the characteristic effect of small particle sizes, as published by Roth et al. [34] and Takasu et al. [35] or for charge transfer between carbon and platinum described by Aricò et al. [36]. The bands that appeared in the second pair of platinum signs, on the other hand, appears around 74.9 and 77.1 eV, which has been reported in the literature to be due to the presence of PtO or PtO_2 [37].

According to the XPS analysis, the Pt concentration at 50 Å of depth was 0.38 wt%, whereas ICP and EDS analyses pointed to a nominal Pt = 0.9 wt% on Pt-CMK-3. This led to the suggestion that the majority of Pt^0 lies inside the nanostructure of the CMK-3 sample. Moreover, about 80 wt% of oxygen was on the outer surface of CMK, with the correspondingly lower amount of not reduced Pt species ($Pt^{2,4+}$).

Figure 15 shows the binding energy for V $2p_{3/2}$ core level of XPS spectra for V-CMK-3. The only one contribution located about 515.0–515.2 eV is assigned to V^{3+} in the form of V_2O_3. Vanadium oxidation states is consistent with XPS spectra previously taken of V_2O_3, which we attributed to $2p_{3/2}$ core electrons [38]. The peak at 525 eV is consistent with the $2p_{1/2}$ peak of vanadium [38].

Vanadium 3^+ has a d^2 electronic configuration and, from inspection of the Tanabe-Sugano diagram for a d^2 ion [39], is expected to have three spin-allowed ground-state absorption transitions in both tetrahedral and octahedral coordination. Therefore, 3^+ is a possible oxidation state of vanadium in CMK-3 according to XPS data.
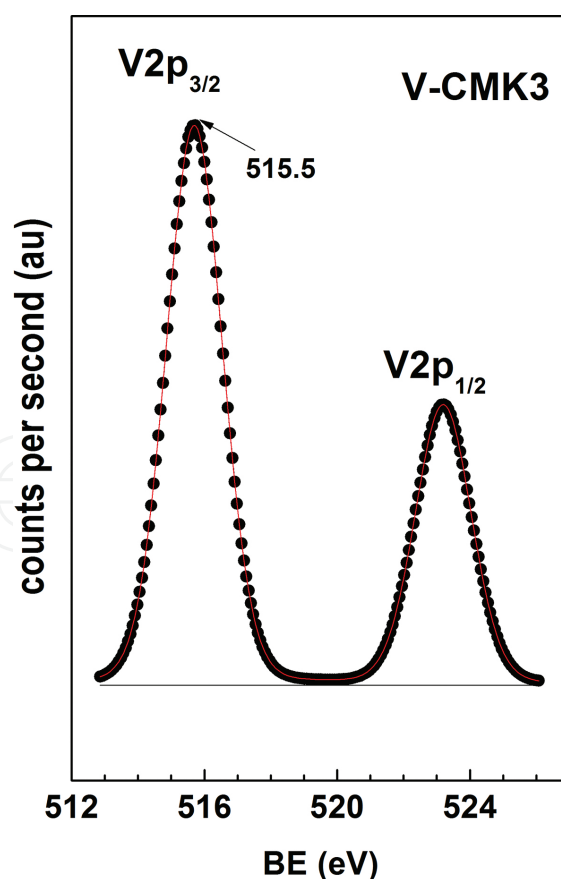

Figure 15. Core level V2p XPS spectra of V-CMK-3.

6. TiO₂-CMK-3 Raman studies

Figure 16 shows Raman spectra of SBA-15, pristine host CMK-3, TiO$_2$-CMK-3, and pure anatase and rutile in the range of 200–1200 cm^{-1}.

For SBA-15, Raman bands at 430, 800 and 1080 cm^{-1} are observed. The bands at 430 and 1080 cm^{-1} can be attributed to symmetric and asymmetric vibrations of the Si-O-Si unit, respectively. The band at 800 cm^{-1} is the symmetric stretching mode of the tetrahedral [SiO$_4$] unit [40–42]. **Figure 16** also shows the spectra of TiO$_2$ onto CMK-3; the characteristic signals of anatase are detected in the sample if compared with those of pure anatase [41,43,44] and pure rutile.

In inset **Figure 16**, we illustrated the Raman spectra of bare CMK-3 and TiO$_2$-CMK-3 (from 1100 to 1700 cm^{-1}). The Raman spectrum of the obtained CMK-3 as well as of TiO$_2$-CMK-3 shows two peaks, at 1578 and 1353 cm^{-1}. The peak at 1578 cm^{-1} corresponds to an E$_2$g mode of graphite and is called G band, related to C=C-double-bonded carbon vibration in hexagonal lattice, while the peak at 1353 cm^{-1} is associated with vibrations of C-C bond, referred to as D band, attributed to the configuration of disordered graphite [45–47]. In the Raman spectrum of graphitic materials such as activated charcoal, carbon black, and CMK, this second line
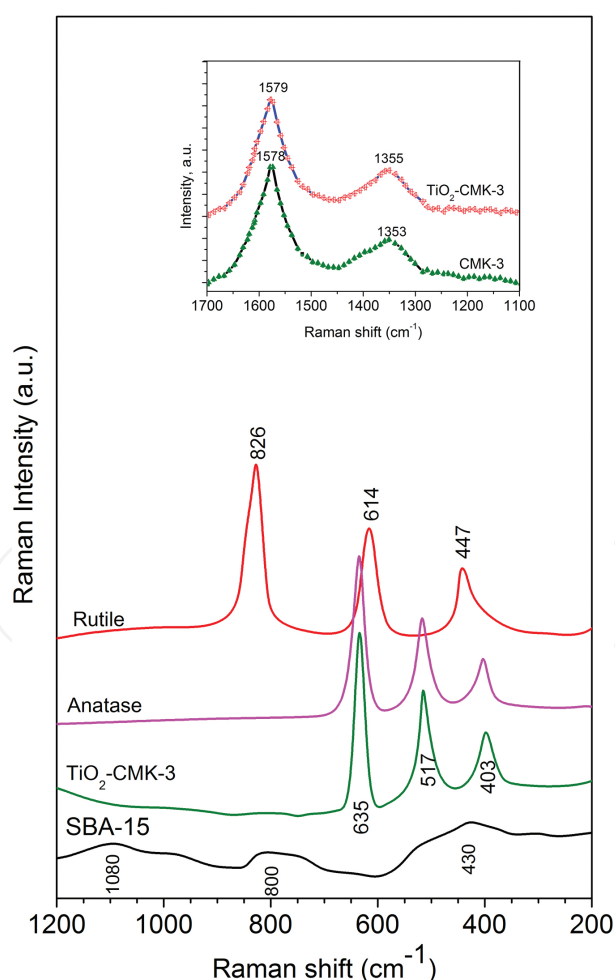

Figure 16. Raman spectra of SBA-15, TiO$_2$–CMK-3, rutile, anatase, and CMK-3 (inset).

appears. The relative intensity of the two lines depends on the type of graphitic material. The intensity of 1353 cm^{-1} line increases with an increase in carbon in the samples and with a decrease in the graphite crystal size. Hence, a signal at 1355 cm^{-1} might possibly be ascribed to a diamond-like atomic arrangement in the graphite samples, probably as partially tetrahedral bonded [48]. This agrees with the proposal of the graphite-like structure for CMK-3 [49]. It could be clearly seen that G and D band intensity of TiO$_2$/CMK-3 was not perturbed significantly (inset **Figure 16**).

7. TEM studies

Figure 17 shows TEM images of CMK-1. Ordered structure was shown to be slightly damaged by thermal treatments.
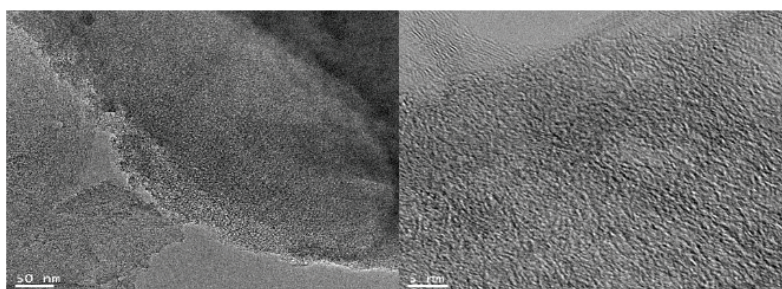

Figure 17. TEM images of CMK-1.

The TEM micrographs of Ni-CMK-1 and Zn-CMK-1 were depicted in **Figure 18**, showing. The ordered cubic Ia3d mesostructure of Metal-CMK-1 (**Figure 18a** and **b**), indicating that the ordered structure of CMK-1 is retained after the incorporation of Ni and Zn nanoparticles.
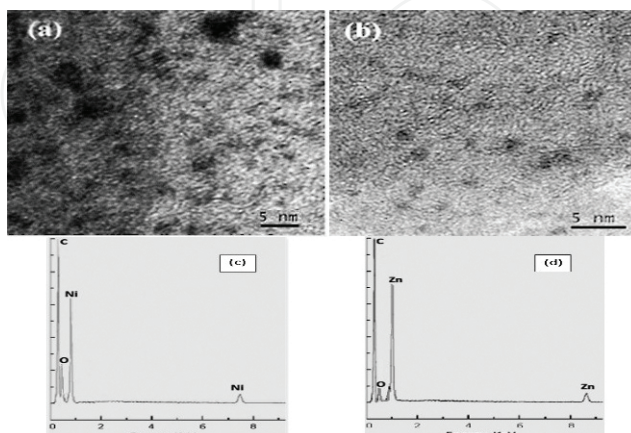

Figure 18. TEM images of (a) Ni-CMK-1 and (b) Zn-CMK-1. (c and d) EDS spectrum of: (c) Ni-CMK-1 and (d) Zn-CMK-1.
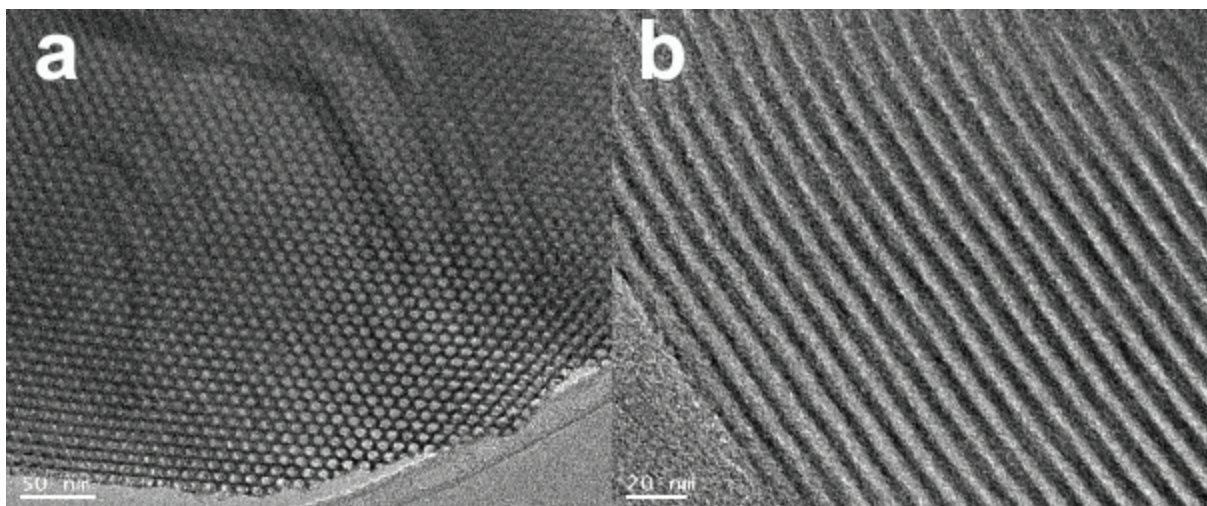
Figure 19. TEM images of SBA-15. (a) [1 0 0] and (b) [1 1 0] reflection planes.

The larger dark areas over the channels most likely correspond to NiO nanoparticle agglomerates on the external surface with average diameter of 11–13 nm (**Figure 18a**). The small dark spots in the image (**Figure 18b**) could be ascribed to Zn and ZnO nanoparticles with average diameter of ~2.5–3 nm probably located into the host pores. EDS analysis was performed to estimate the presence of Zn- and Ni-containing CMK-1. A careful evaluation of the elemental compositions for C, O, and Zn and Ni nanoparticles was performed (**Figure 18c** and **d**).

According to the maps collecting five spots, the average atomic weight % of C, O and Zn nanoclusters in Zn-CMK-1 is about 94.94, 0.26, and 4.80%, respectively. This shows that only 20% of the Zn species appear as ZnO. On the other hand, the average atomic weight % for Ni-CMK-1 was 94.1, 0.6, and 5.3 wt% for C, O, and Ni, clearly indicating that the higher Ni content appears as oxide (about 40%).

Figure 19a shows TEM images of synthesized SBA-15 used as an inorganic template. In **Figure 19b**, an ordered mesoporous array of longitudinal nanochannels can be seen, with pore
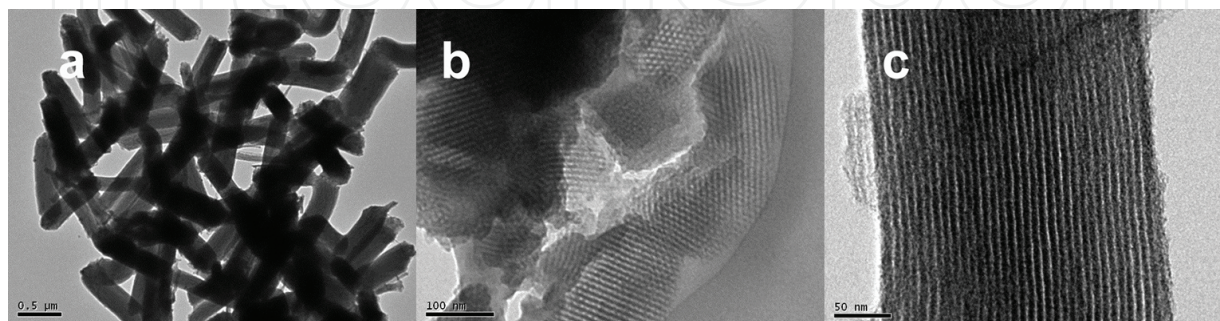

Figure 20. TEM images of CMK-3. (a) Nanoparticles (b) [1 0 0] and (c) [1 1 0] reflection planes.

diameter of 7.5 nm. TEM images of CMK-3 are shown in **Figure 20**. Ordered structure proved to be slightly damaged by thermal treatments and exhibits well-organized pores parallel to one another. The white lines correspond to the mesopores generated in the space where the walls of the SBA-15 template had been.
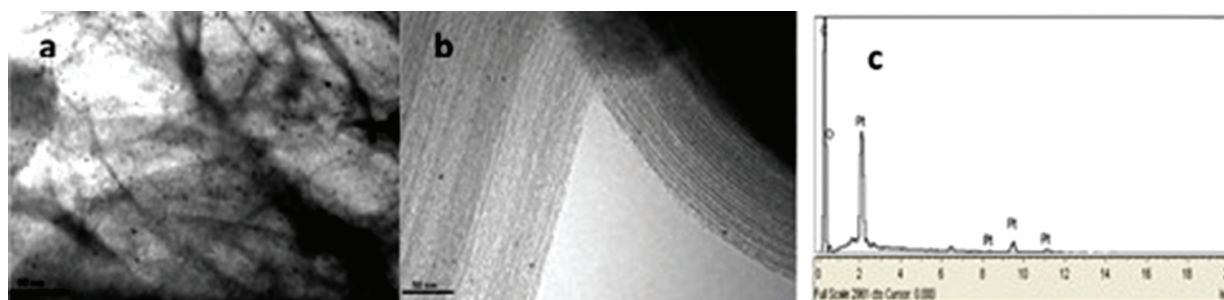

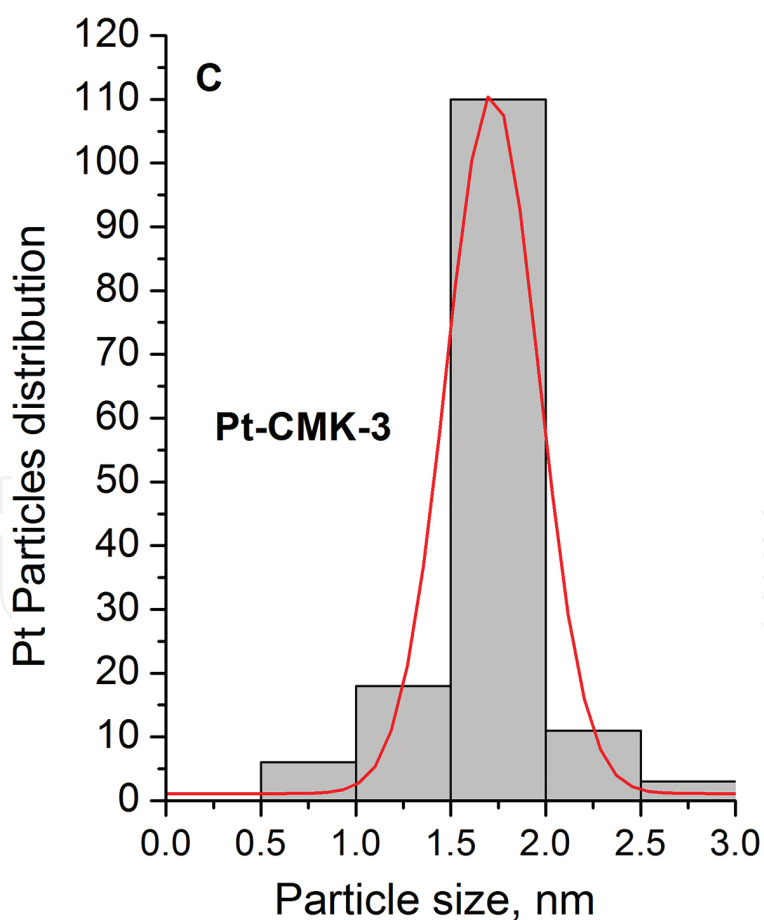**Figure 21.** TEM images (a, b) and EDS (c) spectrum of Pt-CMK-3.

Figure 22. Histograms of PSDs measured from full images of Pt-CMK-3 shown in **Figure 21**.

Figure 21 offers an illustration of TEM micrographs of Pt-CMK-3. The ordered mesostructure of the sample can be seen in **Figure 21a** and **b**, indicating that the ordered structure of CMK-3 persists after Pt nanoparticles are incorporated. The darker contrast (small dark spots) which can be seen in some places may be attributed to the presence of regularly dispersed Pt particles. These images evidence the fine dispersion of Pt^0 on CMK-3, a tinny size dissemination (**Figure 22**), and mean diameter of ~1 to 2 nm inside the mesopores of CMK-3 nanostructure. The existence of Pt^0 inside the pore system of CMK-3 indicates an enhancement in the dispersion phenomena compared with the metal on the external carbon surface. The Pt nanoclusters are active sites for hydrogen adsorption and narrow pore size distribution is vital because the level of dispersion is better and the metal active area is superior.

The metal particles dispersed in CMK-3 carbon have from 1 to 2.5 nm size, and the average particle diameter are approximately to 1.74 nm, showing that utmost of Pt nanoclusters are mainly in the nanostructured intra-channel system of CMK-3.

Dispersion and size distribution of metal particles of Pt toughly depends on the technique of deposition and the characteristics of carbon support as published by Kuppan and Selvam [25], suggesting that reduction with paraformaldehyde of platinum nanoparticles deposited on mesoporous carbon CMK-3 is superior to other methods, including H_2 reduction. In this work, we show that the nature of Pt incorporation to CMK-3 and the preparation of Pt-CMK-3 before Pt reduction (under N_2 atmosphere and controlled temperature removal of the Pt precursor) impact the subsequent size of Pt-reduced nanoparticles, resulting in a narrow distribution of around 1.74 nm (**Figure 22**). If the first elimination of Pt precursors-CMK-3 occurs in an oxidative atmosphere, the likelihood of generating larger Pt clusters increases. Similar consequence on dispersion of iridium over SBA-16 was reported recently [37]. The factor of the Pt source removal (chloroplatinic acid in ethanol-CMK-3) is endothermic and not oxidative under N_2 flow and controlled temperature desorption, avoiding the relocation and accumulation of platinum particles after it reduction.

In order to determine the presence of Pt in the prepared Pt-CMK-3, EDS analysis was employed to carefully evaluate the elemental compositions for C, O, and Pt nanoparticles (**Figure 21c**). Maps of elements were collected from four spots and used to evaluate the presence of all elements. This showed that the average atomic percentage of C, O, and Pt nanoclusters in Pt-CMK-3 is about 98.82, 0.28, and 0.9%, respectively.

TEM images for TiO_2-CMK-3 (**Figure 23**) indicated an ordered structure slightly damaged by thermal treatments; they also exhibit well-organized pores parallel to each other. The white lines correspond to the mesopores generated in the space previously occupied by the walls of SBA-15 template. In **Figure 23b**, a dark spot indicates anatase nanoclusters. **Figure 23c** shows a TEM image with negative contrast, displaying nanoclusters with bright spots, allowing the observation of nanoclusters. Particle size distribution ranged from 1 to 11 nm and mean particle diameter was found to be close to 5 nm, indicating that most of the particles reside within of the pore system.
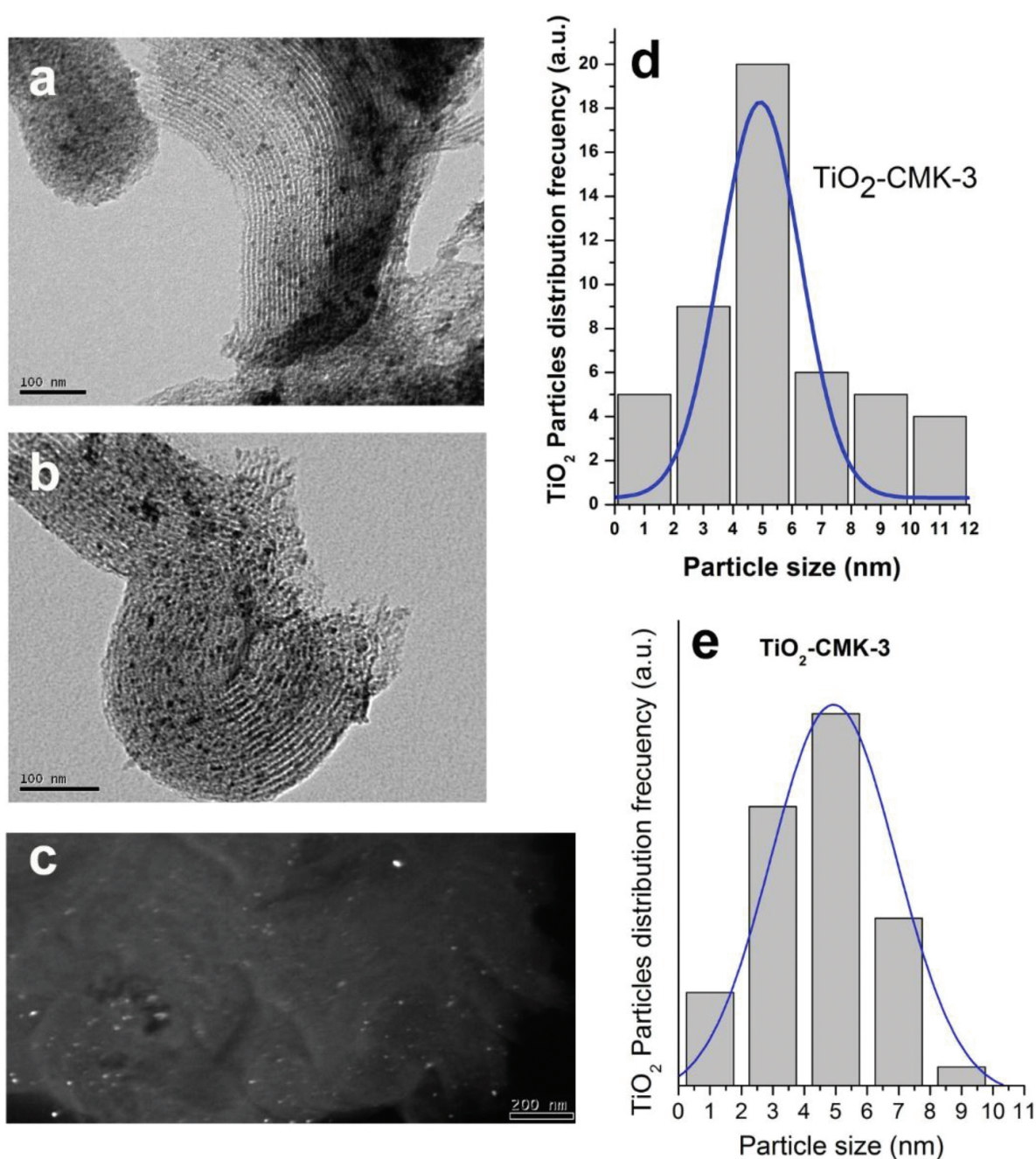
Figure 23. (a) and (b) TEM images TiO$_2$–CMK-3 and (c) Negative contrast image. (d) and (e) particle size distribution histogram corresponding to (a) and (c) TEM images, respectively.

In this work, we show that the nature of TiO$_2$ incorporation into CMK-3 and the preparation of TiO$_2$-CMK-3 (under N$_2$ atmosphere and controlled temperature elimination of Ti precursor), influence posterior TiO$_2$ nanoparticle size, leading to a narrow distribution as shown in the histograms (**Figure 23a** and **c**).

Vanadium nanoclusters were not seen in TEM images of V-CMK-3 due to a low contrast in the TEM image (**Figure 24**).
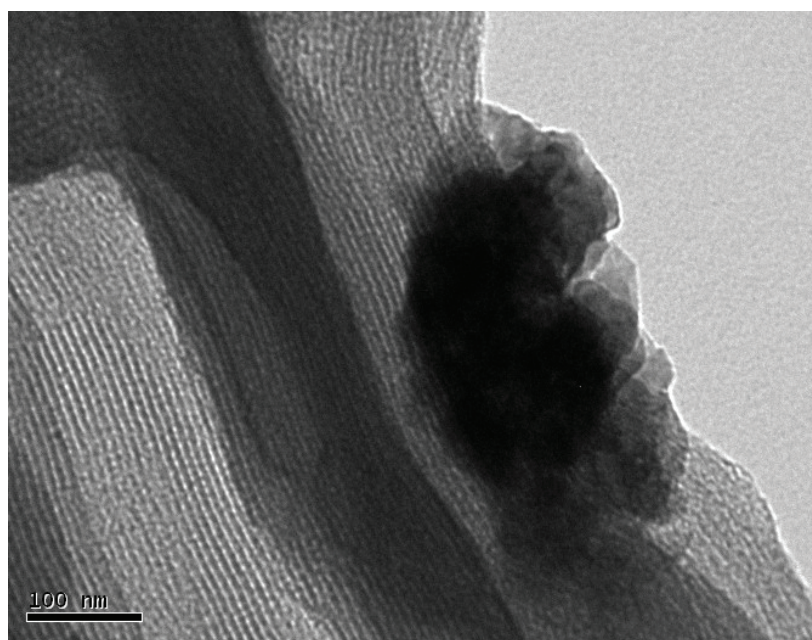
Figure 24. TEM images of V-CMK-3.

8. Hydrogen uptake measurements

The capacity of hydrogen storage was evaluated at low and high pressures and cryogenic temperatures (77 K).

The experimental data were fitted by Freundlich isotherm [50], that is, a purely empirical formula for gaseous adsorbates. The Freundlich model (Eq. (2)) is described by the following equation:

$$Q = K_F \, P^{\frac{1}{n}} \tag{2}$$

Here, Q is the quantity per unit mass of adsorbent, P is the adsorbate pressure, and KF and n are experiential constants (Freundlich constants) for, respectively, adsorbent-adsorbate pair at a constant temperature. A measure of the adsorption intensity is characterized by n, and K_F is the adsorption measurement [50]. This equation was applied to the experimental data using nonlinear least-square regression for arbitrary fit functions and minimizing the objective function by means of the Levenberg-Marquardt method. The fitting accuracy was $R^2 = 0.98$.

The hydrogen storage is defined as "uptake," the carbon material behaves as a sponge, due to the fact that the process is completely reversible and the curve remains in the same place as each point returned to baseline when measurements were carried out without the bath of liquid N_2. We performed the treatment at high temperatures (except TiO_2-CMK-3 sample where treatment is done only under N_2 flow) is to reduce the oxide cluster to a metallic cluster because

the electronic configuration of the metal cluster interacts better with hydrogen molecules and for high H_2 storage. The amount of hydrogen uptake of all samples is higher than carbon samples. The Zn-CMK-1 sample has the highest hydrogen uptake (0–10 bar). Yet, at high pressures, the sample with Zn shows greater H_2 adsorption than all the other samples. In samples that contain metal clusters, there are at least two ways in the process of hydrogen physisorption on metal-CMK-1/CMK-3 surface. Hydrogen molecules spill over onto the CMK-1 nanopores/micropores and are adsorbed onto nanometric metal clusters. Hydrogen adsorption proved to be fully reversible, which indicates that there was no chemical reaction or strong bond between hydrogen and metal nanocluster or the CMK-1 framework.

The proposed mechanism for hydrogen storage in metal-CMK-1/CMK-3 agreed with Kim and Park [51]. Hence, a dipole-induced model is proposed. The first layer of hydrogen molecules could react with the metal cluster because of the high oxidation capacity of metals interacting as dihydrogen complex [35], but the level of this initial interaction is not significant. The second layer of hydrogen molecules is physically adsorbed by dipole-induced interaction. Hydrogen molecules are basically non-polar, but the strong interaction of the metal particles leads to the dipole-induced effects of the hydrogen molecules. The third layer and any other layer above the hydrogen molecules could interact with metal cluster by the same mechanism, but the force of the dipole-induce bond is weak and decreases in inverse proportion with the distance from the surface. Consequently, this mechanism can be applied at higher pressures, since metal-CMK-1/CMK-3 adsorbs a larger amount of hydrogen than carbon at higher pressures.

Theoretically, the 3d states of metals mainly contributed to ground-state electronic structure near the Fermi level of metal-CMK-1 and, to some degree, the p states of carbon. Those contributions of 3d states decrease as we move across the periodic table from Mn to Zn following the increase of d orbital occupancies [52].

Hydrogen bonds to the metal result in an opening of HOMO-LUMO energy gap in the case of Ni-CMK-1, while it shows a reduction in HOMO-LUMO energy gap for Zn-CMK-1, resulting in the appearance of molecular electronic states which allow a better H_2 physisorption.

The understanding at an atomic scale of the hydrogen spillover mechanism for storage of hydrogen in metal-doped carbon materials and metal-organic frameworks is discussed by means of a critical assessment of recent computational and experimental studies. It is claimed that the spillover mechanism includes (a) generation and desorption of mobile H atoms on metal nanoparticles; (b) diffusion of H atoms in weakly bound states on the support; (c) sticking and immobilization of H atoms at preferential locations of the receptor where barriers to sticking are lower, and (d) Eley-Rideal recombination of the adsorbed H atoms with diffusing mobile H atoms to form H_2 [53].

In the TiO_2-CMK-3, surface can adsorb hydrogen molecules by spill over onto CMK-3 nano-pores/micropores and adsorbed onto nanometric anatase clusters. First, we could attribute this adsorption to the different particle surface areas, since the adsorbed quantity might be primarily related to the available free surface area. Second, we could attribute it to the fact that nanometric carbon promoting the high-surface areas of TiO_2 nanoclusters. CMK-3 surface promotes the high-surface areas of TiO_2 nanoclusters may possibly modify oxidation state and

control porosity feature, which is important to cause hydrogen adsorption (H_2 molecules) by weak chemical pathways (such as dihydrogen complex interaction), although anatase or rutile is generally weak in hydrogen storage [54]. Through XRD and TEM observation, we also noticed that with the assistance of CMK-3, the fabricated TiO_2 nanoparticles show small size and high dispersion, contributing to the substantial increase in H_2 adsorption. In other words, the presence of TiO_2 nanoclusters in CMK-3 results in formation of better-localized states of electrons at TiO_2 nanoclusters and CMK-3 interface. These localized states may distribute electron concentration at the surface of TiO_2-CMK-3 composite and causes a few reactions between hydrogen molecules and surface TiO_2 nanoclusters [54]. According to theoretical investigations [55], TiO_2 and CMK-3 interaction is not affected by the physisorption of the first H_2 molecule because it does not impact the distance between Ti and the nearest C. The H-H distance is influenced (elongated) by bonds Ti-C sp2d because the strong repulsive phenomena on the adsorbed H_2. The hydrogen atoms of the adsorbed H_2 molecule should have negative charges, and the H_2 molecule can be regarded as trapped by Ti cation by means of the charge polarization mechanism. This is an indicator that Ti donates electrons to the nearest C atoms on CMK-3, where the d-orbitals of the Ti atom overlap the sp^2 orbitals of the Ti-C bonds to form the mixed sp^2d hybridization. This charge transfer is possible because the Ti atom is in cationic form and renders extensive hetero-polar bonding between the Ti atom and its neighboring C atoms, resulting in an increase in H_2 molecule uptake. Moreover, CMK-3 approaching the positively charged Ti cation leads to loss of d-orbital degeneracy since the electrons of CMK-3 will be closer to some d-orbitals while being farther away from others. Thus, those d-orbitals that are closer to CMK-3 have a higher degree of energy than those farther away. This results in d-orbitals splitting in energy to reduce the total energy and stabilize the system, as explained by the ligand field theory [56].

Therefore, the first layer of hydrogen molecules could be reacted with the metal cluster due to high oxidation/reduction metals capacity interacting like as dihydrogen complex [35], similar metal-carbon samples; yet, the amount of this initial interaction is negligible. The second layer of hydrogen molecules is physically adsorbed by dipole-induced interaction as metal-carbon samples. Hydrogen molecules are non-polar, but the strong interaction of anatase particles leads to dipole-induced effects in H_2. The third level of the layers and any higher layer of H_2 molecules could bond with metal cluster by the same way; however, the dipole-induced interaction is weak, decreasing as separation to the surface increases. At higher pressure, this mechanism can be applied; consequently, the adsorption of hydrogen to TiO_2-CMK-3 is higher than CMK-3 at greater pressures. The understanding of the distribution of frontier molecular orbitals around a nanostructure would be a significant guideline to design new functionalized materials for hydrogen storage. While strong localization of the highest occupied molecular orbital (HOMO) occurs on Ti cation located at the surface on anatase nanocluster, strong delocalization of the lowest unoccupied molecular orbital (LUMO) occurs at the base area. The strong localization of HOMO on Ti cation at the surface explains the enhanced adsorption interactions of H_2 molecules [55]. Moreover, hydrogen bonds to anatase result in an opening of HOMO-LUMO energy gap. A reduction in HOMO-LUMO energy gap for TiO_2-CMK-3 results in the appearance of molecular electronic states that allow a better H_2 physisorption [52].

The hydrogen storage on V-CMK-3 sample could be attributed to a high V_2O_3 particle surface areas and could be attributed to the fact that nanometric carbon helping the high-surface areas of V_2O_3 nanoclusters. However, the high hydrogen adsorption may be explain because hydrogen storage might increase via the spill-over phenomenon. Specifically, hydrogen molecules are dissociated on the surface of the introduced transition metal cation (V^{+3}). The other potential explanation is that the hydrogen molecules are attracted into the graphite pores due to formed weak dipoles with V_2O_3 nanoclusters. Metal cation increases and quickens hydrogen storage through a weak chemical reaction (from either the spill-over phenomenon or dipole attraction) (**Figure 25**).
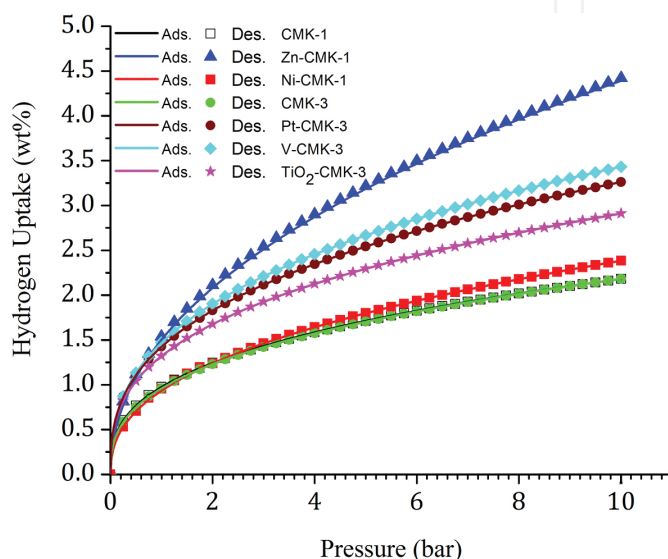

Figure 25. Isotherms of hydrogen at 77 K on the different materials studied at a range of pressures (0–10 bar).
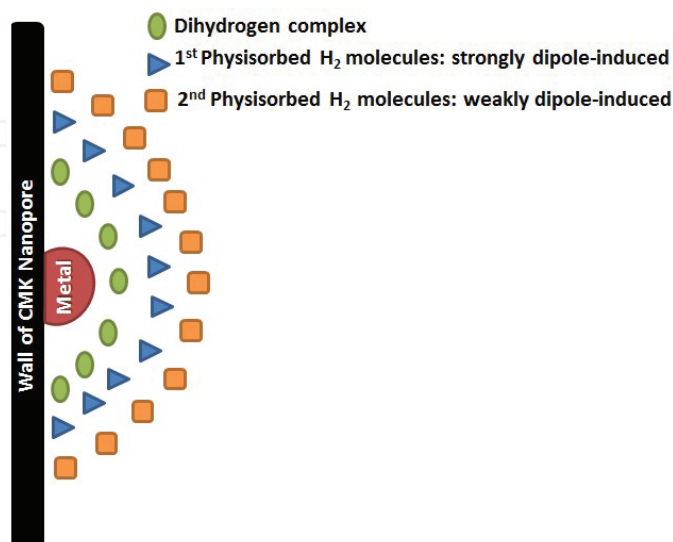

Figure 26. Scheme for the proposed mechanism of metal-CMK and hydrogen interaction.

The scheme showed in **Figure 26** suggests a mechanism for hydrogen storage in carbon mesoporous CMK, modified with metals in agreement with Kim et al.

9. Conclusions

We have shown that a hopeful hydrogen storage material can be obtained by ordered porous carbons CMK-1/CMK-3 modified with Ni, Zn, Pt, Ti, and V species that were synthesized by replication using MCM-48 and SBA-15 as hard template, respectively. The metal-metal/oxide nanoparticles-containing carbon was obtained by wetness impregnation considering the thermal treatments employing H_2. Zn species mostly found as metallic Zn while Ni as NiO, with the highest average cluster size (12 nm), indicating greater dispersion of zinc and its incorporation in the nanoporous of mesoporous carbons but without occlusion by their small size compared with NiO clusters. The higher Zn dispersion probably causing a high metal surface area and a better use of the support allowed to a superior performance to H_2 uptake of Zn-CMK-1. Pt-CMK-3 sample present an improvement in the capacity of hydrogen uptake than CMK-3 carbon due to the better dispersion of uniform platinum nanoparticles as well as better utilization of the support, which may probably was originate of a high-surface area and pore volume, that allow a large dispersion of Pt. Pt nanoparticles in Pt-CMK-3 have smaller size (~1.7 nm average) and have a quite well dispersion inside the nanochannels of CMK-3. This shows the better hydrogen uptake of the Pt-CMK-3 than CMK-3 carbon.

TiO_2-CMK-3 can significantly enhance hydrogen adsorption capacity and hydrogen storage performance of CMK-3 material, proving to prospective candidates for application in hydrogen storage. CMK-3 modified with TiO_2 in anatase phase shows an enhanced capacity for H_2 storage than that of the nanoporous CMK-3 sample. TiO_2-CMK-3 improved performance and larger activity for H_2 uptake is attributed to improved dispersion of uniform anatase nanoparticles in addition to efficient use of the CMK-3, probably originate in the high pore volume and surface area, allowing a great dispersion of anatase. TiO_2 (anatase phase) nanoparticles in TiO_2-CMK-3 have a smaller size (~5 nm average, obtained by XRD and TEM) and a quite good dispersion.

Vanadium-modified carbon sample has higher hydrogen storage than CMK-3 pristine material and is the best material for hydrogen adsorption using CMK-3 nanometric carbon as support but lower than Zn-CMK-1.

A hydrogen uptake mechanism on metal/carbon surfaces was proposed. We can conclude by indicating that CMK-1/CMK-3 hydrogen storage capacity was increased by addition of metal clusters. Moreover, hydrogen storage behaviors onto metal/metal oxides-carbons can be optimized by controlling the metal cluster size and dispersion and by increasing the carbon-specific surface area.

Acknowledgements

Author details

Marcos B. Gómez Costa, Juliana M. Juárez and Oscar A. Anunziata[*]

*Address all correspondence to: oanunziata@scdt.frc.utn.edu.ar

Centre for Research in Nanoscience and Nanotechnology (NANOTEC), Cordoba Regional Faculty, National Technological University, Maestro López y Cruz Roja Argentine, Córdoba, Argentina

References

[1] Schlapbach L, Züttel A. Hydrogen-storage materials for mobile applications. Nature. 2001; 414: 353–358.

[2] Kajiura H, Tsutsui S, Kadono K, Kakuta M, Ata M, Murakami Y. Hydrogen storage capacity of commercially available carbon materials at room temperature. Applied Physics Letters. 2003; 82: 1105–1107.

[3] Mandoki NT, Dentzer J, Piquero T, Saadallah S, David P, Guterl CV. Hydrogen storage in activated carbon materials: role of the nanoporous texture. Carbon. 2004; 42: 2744–2747.

[4] Züttel A, Sudan P, Mauron P, Kiyobayashi T, Emmenegger C, Schlapbach L. Hydrogen storage in carbon nanostructures. International Journal of Hydrogen Energy. 2002; 27: 203–212.

[5] Fang G, Liu G, Yang Y, Wang S. Quartz crystal microbalance sensor based on molecularly imprinted polymer membrane and three-dimensional Au nanoparticles@mesoporous carbon CMK-3 functional composite for ultrasensitive and specific determination of citrinin. Sensors and Actuators B. 2016; 230: 272–280.

[6] Gadiou R, Saadallah SE, Piquero T, David P, Parmentier J, Guterl CV. The influence of textural properties on the adsorption of hydrogen on ordered nanostructured carbons. Microporous and Mesoporous Materials. 2005; 79: 121–128.

[7]   Fang BZ, Zhou HS, Honma I. Ordered porous carbon with tailored pore size for electrochemical hydrogen storage application. The Journal of Physical Chemistry B. 2006; 110: 4875–4880.

[8]   Zhai Y, Dou Y, Zhao D, Fulvio PF, Mayes RT, Dai S. Carbon materials for chemical capacitive energy storage. Advanced Materials. 2011; 23: 4828–4850.

[9]   Yang ZX, Xia YD, Sun XZ, Mokaya R. Preparation and hydrogen storage properties of zeolite-templated carbon materials nanocast via chemical vapor deposition: effect of the zeolite template and nitrogen doping. The Journal of Physical Chemistry B. 2006; 110: 18424–18431.

[10] Wegrzyniak A, Jarczewski S, Wach A, Hedrzak E, Kustrowski P, Michorczyk P. Catalytic behaviour of chromium oxide supported on CMK-3 carbon replica in the dehydrogenation propane to propene. Applied Catalysis A: General. 2015; 508: 1–9.

[11] Anbia M, Parvin Z. Desulfurization of fuels by means of a nanoporous carbon adsorbent. Chemical Engineering Research and Design. 2011; 89: 641–647.

[12] Juárez JM, Gómez Costa MB, Anunziata OA. Synthesis and characterization of Pt-CMK-3 hybrid nanocomposite for hydrogen storage. International Journal of Energy Research. 2015; 39: 128–139. doi:10.1002/er.3229.

[13] Juárez JM, Gómez Costa MB, Anunziata OA. Preparation and characterization of activated CMK-1 with Zn and Ni species applied in hydrogen storage. International Journal of Energy Research. 2015; 39: 941–953. doi:10.1002/er.3298.

[14] Benhamou A, Basly JP, Baudu M, Derriche Z, Hamacha R. Amino-functionalized MCM-41 and MCM-48 for the removal of chromate and arsenate. Journal of Colloid and Interface Science. 2013; 404: 135–139.

[15] Jorda-Beneyto M, Lozano-Castello D, Suarez-Garcia F, Cazorla-Amoros D, Linares-Solano A. Advanced activated carbon monoliths and activated carbons for hydrogen storage. Microporous and Mesoporous Materials. 2008; 112: 235–242.

[16] Valles VA, Ledesma BC, Rivoira LP, Cussa J, Anunziata OA, Beltramone AR. Experimental design optimization of the tetralin hydrogenation over Ir–Pt-SBA-15. Catalysis Today. 0920–5861. doi:10.1016/j.cattod.2015.07.018. Article in press. Available on line at http://www.sciencedirect.com/science/article/pii/S0920586115004095

[17] Ryoo R, Joo SH, Jun S. Synthesis of highly ordered carbon molecular sieves via template-mediated structural transformation. Journal of Physical Chemistry B. 1999; 103:7743–7746.

[18] Solovyov LA, Zaikovskii VI, Shmakov AN, Belousov OV, Ryoo R. Framework characterization of mesostructured carbon CMK-1 by X-ray powder diffraction and electron microscopy. Journal of Physical Chemistry B. 2002; 106: 12198–12202.

[19] Huwe H, Fröba M. Iron (III) oxide nanoparticles within the pore system of mesoporous carbon CMK-1: intra-pore synthesis and characterization. Microporous and Mesoporous Materials. 2003; 60: 151–158.

[20] Suryavanshi U, Iijima T, Hayashia A, Hayashi Y, Tanemura M. Fabrication of ZnO nanoparticles confined in the channels of mesoporous carbon. Chemical Engeneering Journal. 2012; 179: 388–393.

[21] Habibi MH, Rahmati MH. Fabrication and characterization of ZnO@CdS core–shell nanostructure using acetate precursors: XRD, FESEM, DRS, FTIR studies and effects of cadmium ion concentration on band gap. Spectrochimica Acta Part A: Molecular and Biomolecular Spectroscopy. 2014; 133: 13–18.

[22] Chen R, Han J, Yan X, Zou C., Bian J, Alyamani A, Gao W. Photocatalytic activities of wet oxidation synthesized ZnO and ZnO–TiO$_2$ thick porous films. Applied Nanoscience. 2011; 1: 37–44.

[23] Gómez Costa MB, Juárez JM, Martínez ML, Beltramone AR, Cussa J, Anunziata OA. Synthesis and characterization of conducting polypyrrole/SBA-3 and polypyrrole/Na-AlSBA-3 composites. Material Reseach Bulletin. 2013; 48: 661–667.

[24] Veena Gopalan E, Malini KA, Santhoshkumar G, Narayanan TN, Joy PA, Al-Omari IA, Sakthi Kumar D, Yoshida Y, Anantharaman MR. Template-assisted synthesis and characterization of passivated nickel nanoparticles. Nanoscale Research Letters. 2010; 5: 889–897.

[25] Kuppan B, Selvam P. Platinum-supported mesoporous carbon (Pt/CMK-3) as anodic catalyst for direct methanol fuel cell applications: the effect of preparation and deposition methods. Progress in Natural Science: Materials International. 2012; 22(6): 616–623.

[26] Wilkerson RJ, Elder T, Sowinksi O, Fostvedt JI, Hoefelmeyer JD. Phase transfer of oleic acid stabilized rod-shaped anatase TiO$_2$ nanocrystals. Surface Science. 2016; 648: 333–338.

[27] Langford JI, Wilson AJC. Scherrer after sixty years: a survey and some new results in the determination of crystallite size. Journal of Applied Crystallography. 1978; 11: 102–113.

[28] van Huis MA, van Veen A, Schut H, Eijt SWH, Kooi BJ, De Hosson JTM. Structural properties of Au and Ag nanoclusters embedded in MgO. Nuclear Instruments and Methods in Physics Research Section B. 2002; 191: 442–446.

[29] Biesinger MC, Lau LWM, Gerson AR, Smart RSC. Resolving surface chemical states in XPS analysis of first row transition metals, oxides and hydroxides: Sc, Ti, V, Cu and Zn. Applied Surface Science. 2010; 257: 887–898.

[30] Wöll C. The chemistry and physics of zinc oxide surfaces. Progress in Surface Science. 2007; 82: 55.

[31] Kónya Z, Vesselényi I, Kiss J, Farkas A, Oszkó A, Kiricsi I. XPS study of multiwall carbon nanotube synthesis on Ni-, V-, and Ni, V-ZSM-5 catalysts. Applied Catalysis A: General. 2004; 260(1):55–61.

[32] Loviat F, Czekaj I, Wambach J, Wokaun A. Nickel deposition on γ-Al$_2$O$_3$ model catalysts: an experimental and theoretical investigation. Surface Science. 2009; 603(14): 2210–2217.

[33] Contour JP, Mouvier G, Hoogewijs M, Leclere C. X-ray photoelectron spectroscopy and electron microscopy of PtRh gauzes used for catalytic oxidation of ammonia. Journal of Catalysis. 1977; 48: 217–228.

[34] Roth C, Goetz M, Fuess H. Synthesis and characterization of carbon-supported PteRueWOx catalysts by spectroscopy and diffraction methods. Journal of Applied Electrochemistry. 2001; 31: 793–798.

[35] Takasu Y, Unwin R, Tesche B, Bradshaw AM, Grunze M, Photoemission from palladium particle arrays on an amorphous silica substrate. Surface Science. 1978; 77: 219–232.

[36] Aricò AS, Antonucci V, Giordano N, Shukla AK, Ravikumar MK, Roy A, Barman SR, Sarma DD, Methanol oxidation on carbon-supported platinum–tin electrodes in sulfuric acid. Journal of Power Sources. 1994; 50: 295–309.

[37] Ledesma BC, Vallés VA, Rivoira LP, Martínez ML, Anunziata OA, Beltramone AR. Hydrogenation of tetralin over Ir catalysts supported on titania-modified SBA-16. Catalysis Letters. 2014; 144: 1–13.

[38] Sawatzky GA, Post D. X-ray photoelectron and Auger spectroscopy study of some vanadium oxides. Physical Review B. 1979; 20: 1546–1555.

[39] Sugano S, Tanabe Y, Kamimura H. Multiplets of transition-metal ions in crystals. Academic Press, New York (1970).

[40] Bassi AL, Cattaneo D, Russo V, Bottani C E, Barborini E, Mazza T, Piseri P, Milani P, Ernst FO, Wegner K, Pratsinis SEJ. Raman spectroscopy characterization of titania nanoparticles produced by flame pyrolysis: the influence of size and stoichiometry. Journal of Applied Physics. 2005; 98: 74305.

[41] Balaji S, Djaoued Y, Robichaud J. Phonon confinement studies in nanocrystalline anatase-TiO$_2$ thin films by micro Raman spectroscopy. Journal of Raman Spectroscopy. 2006; 37: 1416–1422.

[42] Mazza T, Barborini E, Piseri P, Milani P, Cattaneo D, Bassi AL, Bottani CE, Ducati C. Raman spectroscopy characterization of TiO$_2$ rutile nanocrystals. Physical Review B: Condensed Materials. 2007; 75: 045416.

[43] Konatowski J, Wichterlova B, Jitkovsky J, Loffler E, Pilz W. Spectroscopic studies of vanadium-substituted zeolitic silicates of MFI topology. Journal of the Chemical Society: Faraday Transactions. 1996; 92: 1067–1078.

[44] Yang Q, Wang S, Lu J, Xiong G, Feng ZC, Xin Q, Li C. Epoxidation of styrene on Si/Ti/SiO2 catalysts prepared by chemical grafting. Applied Catalysis A: General. 2000; 194: 507–514.

[45] Dresselhaus MS, Jorio A, Hofmann M, Dresselhaus G, Saito R. Perspectives on carbon nanotubes and graphene Raman spectroscopy. Nano Letters. 2010; 10: 751–758.

[46] Lu J, Yang J, Wang J, Lim A, Wang S, Loh KP. One-pot synthesis of fluorescent carbon nanoribbons, nanoparticles, and graphene by the exfoliation of graphite in ionic liquids. ACS Nano. 2009; 3: 2367–2375.

[47] Zhang W, Cui J, Tao C, Wu Y, Li Z, Ma L, Wen Y, Li G. A strategy for producing pure single-layer graphene sheets based on a confined self-assembly approach. Angewandte Chemie. 2009; 121: 5978–5982.

[48] Tuinstra F, Koenig JL. Raman spectrum of graphite. The Journal of Chemical Physics. 1970; 53: 1126–1130.

[49] Darmstadt H, Roy C, Kaliaguine S, Choi SJ, Ryoo R. Surface chemistry of ordered mesoporous carbons. Carbon. 2002; 40: 2673–2683.

[50] Zeinaldi F, Ghoreyshi AA, Najafpour GD. Adsorption of dichloromethane from aqueous phase using granular activated carbon: isotherm and breakthrough curve measurements. Middle East Journal Science Research. 2010; 5(4): 191–198.

[51] Kim B-J, Park S-J. Optimization of the pore structure of nickel/graphite hybrid materials for hydrogen storage. International Journal of Hydrogen Energy. 2011; 36: 648–653.

[52] Nguyen TQ, Bustria Padama AA, Sison Escano MC, Kasai, H. Theoretical study on the adsorption of NO on metal macrocycles, metal = Mn,Fe,Co,Ni,Cu,Zn. ECS Transactions. 2013; 45(20): 91–100.

[53] Psofogiannakisa GM, Froudakis GE. Fundamental studies and perceptions on the spillover mechanism for hydrogen storage. Chemical Communications. 2011; 47: 7933–7943.

[54] Hoang Tuan KA, Antonelli David M. Exploiting the Kubas interaction in the design of hydrogen storage materials. Advanced Materials. 2009; 21: 1787–1800.

[55] Shalabi AS, Taha HO, Soliman KA, Abeld S. Hydrogen storage reactions on titanium decorated carbon nanocones theoretical study. Journal of Power Sources. 2014; 271: 32–41.

[56] Zhang LP, Wu P, Sullivan MB. Hydrogen Adsorption on Rh, Ni, and Pd Functionalized single-walled boron nitride nanotubes. Journal of Physical Chemistry C. 2011; 115: 4289–4296.